2017-12-01

Quantitative Morphological Classification of Planetary Craterforms Using Multivariate Methods of Outline-Based Shape Analysis

Thomas Joseph Slezak
Brigham Young University

Quantitative Morphological Classification of Planetary Craterforms

Using Multivariate Methods of Outline-Based Shape Analysis

Thomas Joseph Slezak

A thesis submitted to the faculty of
Brigham Young University
in partial fulfillment of the requirements for the degree of

Master of Science

Jani Radebaugh, Chair
Mark C. Belk
Eric H. Christiansen
Bart J. Kowallis

Department of Geological Sciences

Brigham Young University

ABSTRACT

Quantitative Morphological Classification of Planetary Craterforms
Using Multivariate Methods of Outline-Based Shape Analysis

Thomas Joseph Slezak
Department of Geological Sciences, BYU
Master of Science

Craters formed by impact and volcanic processes are among the most fundamental planetary landforms. This study examines the morphology of diverse craterforms on Io, the Moon, Mars, and Earth using quantitative, outline-based shape analysis and multivariate statistical methods to evaluate the differences between different types of. Ultimately, this should help establish relationships between the form and origin of craterforms. Developed in the field of geometric morphometrics by paleontological and biological sciences communities, these methods were used for the analysis of the shapes of crater outlines.

The shapes of terrestrial ash-flow calderas, terrestrial basaltic shield calderas, martian calderas, Ionian paterae, and lunar impact craters were quantified and compared. Specifically, we used circularity, ellipticity, elliptic Fourier analysis (EFA), Zahn and Roskies (Z-R) shape function, and diameter. Quantitative shape descriptors obtained from EFA yield coefficients from decomposition of the Fourier series that separates the vertical and horizontal components among the outline points for each shape. The shape descriptors extracted from Z-R analysis represent the angular deviation of the shapes from a circle. These quantities were subjected to multivariate statistical analysis including principal component analysis (PCA) and discriminant analysis, to examine maximum differences between each *a priori* established group.

Univariate analyses of morphological quantities including diameter, circularity, and ellipticity, as well as multivariate analyses of elliptic Fourier coefficients and Z-R shape function angular quantities show that ash-flow calderas and paterae on Io, as well as basaltic shield calderas and martian calderas, are most similar in shape. Other classes of craters are also shown to be statistically distinct from one another. Multivariate statistical models provide successful classification of different types of craters. Three classification models were built with overall successful classification rates ranging from 90% to 75%, each conveying different shape information. The EFA model including coefficients from the 2^{nd} to 10^{th} harmonic was the most successful supervised model with the highest overall classification rate and most successful predictive group membership assignments for the population of examined craterforms.

Multivariate statistical methods and classification models can be effective tools for analyzing landforms on planetary surfaces and geologic morphology. With larger data sets used to enhance supervision of the model, more successful classification by the supervised model could likely reveal clues to the formation and variables involved in the genesis of landforms.

Keywords: planetary geology, volcanology, geomorphology, shape analysis, geometric morphometrics, remote sensing, image processing, multivariate statistics, geomorphology

ACKNOWLEDGEMENTS

I appreciate the support provided to me over the past 2.5 years from my parents, sister, grandparents, cousins, BYU's Geological Sciences Department, and my advisors and committee. I appreciate the guidance provided by my advisor, Jani Radebaugh, and my committee members, especially Eric Christiansen for adopting me and the challenges of my research in times of necessity. Additionally, I acknowledge the resources, constructive dialog, and support of my work by various members in multiple disciplines of the academic community, particularly Norm MacLeod, Prasun Mahanti, and William Christensen. I thank the Brigham Young University Graduate School and Graduate Student Society and the Geological Society of America Rocky Mountain Division for travel funding support. I am grateful for the opportunities and experiences provided to me through internships that have sustained my enthusiasm and enhanced my technical skills for research in planetary science with Laz Kestay, Ashley Davies, and David Kring. I appreciate those who initiated, inspired and further encouraged my pursuit of knowledge in planetary studies including Mark Robinson, Austin Godber, Phil Christensen, Jim Bell, and many others. I thank all those who have benevolently supported me, personally and professionally, through the unique challenges that have accompanied this project.

TABLE OF CONTENTS

LIST OF TABLES

LIST OF FIGURES

1 INTRODUCTION

1.1 The Problem

The morphology of craterforms on a planetary surface provides the primary source of information used to infer the geologic history of the body (Zimbelman, 2001). Despite substantial conceptual and mathematical development in the quantitative methods used in the analysis of natural, irregular forms (e.g., Zahn and Roskies, 1972; Kuhl and Giardina, 1982; Lohmann, 1983; Rohlf and Marcus, 1993), modern studies of planetary landforms (Michalski and Bleacher, 2013; Watters et al., 2017) continue to employ methods of morphometric analysis, such as measurement-derived dimensionless ratios or "indices", abandoned as tools for useful morphologic analysis by the biological shape analysis community in the 1970s (Lestrel, 2000).

Analogous to biology, examinations of form in geology aim to reveal how mechanics and evolution relate to morphology; together these fields comprise the physical natural sciences (Lestrel, 2000; Neal and Russ, 2012). One example of a geological form is a craterform, or roughly round depression. Craterforms, circular to sub-circular to sub-angular depressions of no implied origin, similar in morphology can be produced from different processes (Evans, 1986), and physical processes inferred from qualitative information lacking quantitative support is more likely to conject incorrect conclusions (Hayek, 1979), many of which are used to understand the global evolution and geologic history of a planetary body (Greeley, 2013).

The links between morphology, origin, and the processes incurred on a natural form are evident in geology ranging in scale from millimeter to meter-sized sedimentary particles (Powers, 1953) to planetary landforms (Zimbelman, 2001) ranging in scale from meters to hundreds of kilometers.

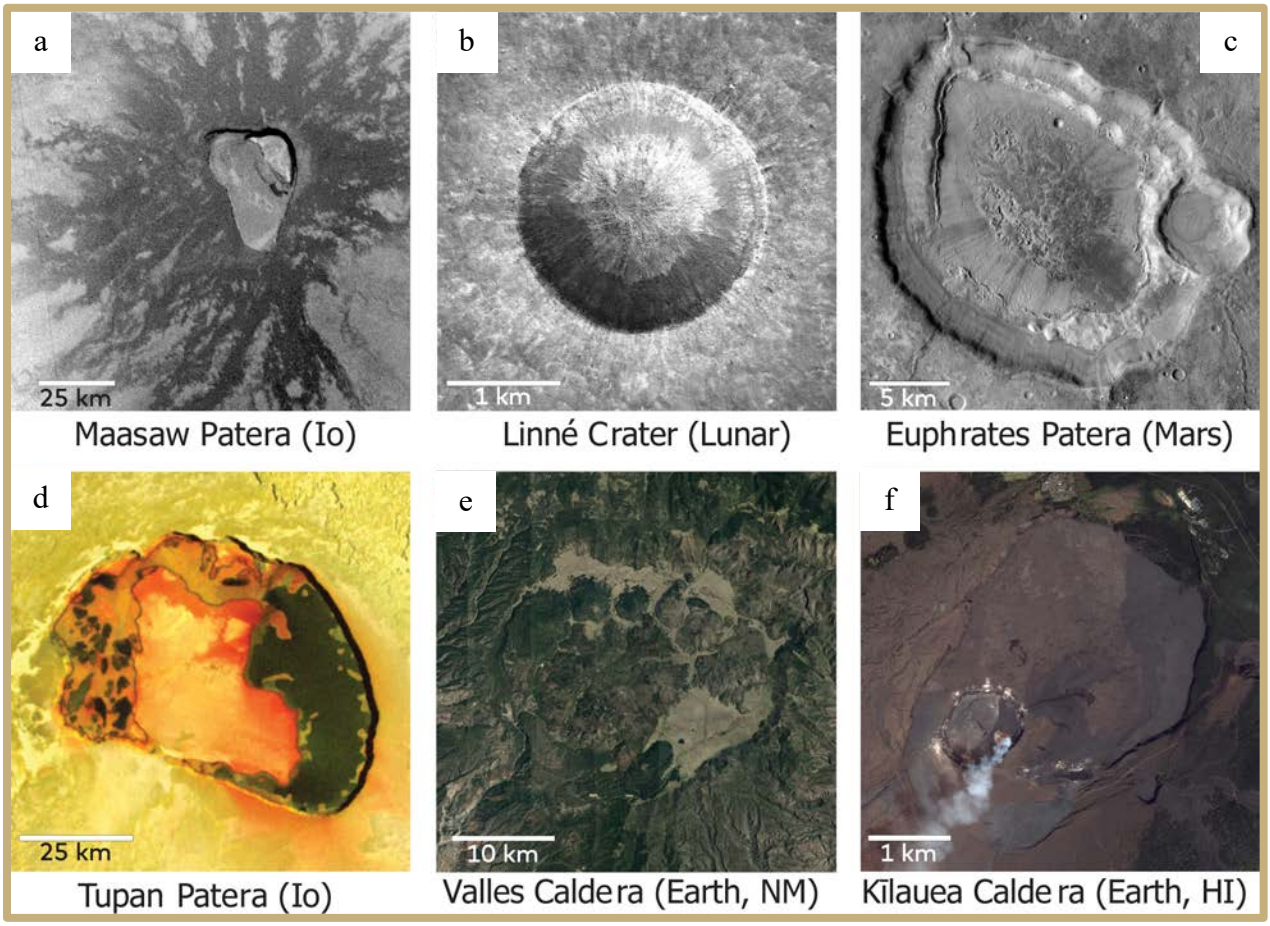

Figure 1 Examples of craterforms examined in this study including paterae on Io (a and d), lunar impact craters (b), martian calderas (c), terrestrial ash-flow calderas (e) and basaltic shield volcanoes (f). While the crater morphologies are similar, differences in shape can be quantitatively derived.

However, shape is not easily quantified and communicating the information provided by morphology can be difficult. Existing methods used to differentiate landforms and assign respective nomenclature use criteria such as qualitative descriptions, indices derived from measurements (e.g., width to length ratio), and the fitting of mathematical models (e.g., power laws, quadratic equations) to evaluate landforms using morphologic variables (Evans, 1986).

However, it is likely that the morphology of surface forms produced by natural processes is multivariate (Evans, 1972).

This study introduces multivariate, outline-based shape analysis as a quantitative tool to support the classification of planetary landforms. We adapt methods from modern studies in systematic evolutionary biology and paleontology that are used to identify or classify species from differences in form. Quantitative support for visual assessments of morphologic phenomena in geology enhance the scientific interpretations extracted from observations (MacLeod, 2002). Both historical (Evans, 1972) and contemporary (Pike, 2001; Mahanti et al., 2014) works have stressed the importance of establishing a standardized quantitative classification system for the morphologic characterization of geologic landforms, yet no such system currently exists for the various types of craters formed on planets and moons.

Craterforms (see Fig. 1) are found on all planetary bodies throughout the solar system. The variables and processes that influence the resultant morphologies, or shapes, of craterforms present a morphogenetic link. While the shapes of some craterforms such as lunar impact craters are relatively simple, others such as paterae (defined by the International Astronomical Union as "complex, or irregular craters with scalloped edges") on Io are complex and the processes of their formation remain incompletely understood (Radebaugh et al., 2001; Radebaugh, 2005; Slezak et al., 2015; Dundas, 2017). Others, such as lunar impact craters have been well studied, with differences in their morphology already quantitatively linked to differences in formation (Wilhelms et al., 1987; Melosh, 1989).. We quantify the two-dimensional crater shapes from images using digitized coordinates of their outlines. A wealth of information is stored in the morphology of geologic forms and this study examines this information using modern methods of morphometrics previously unapplied to studies of planetary surfaces. This work provides a

framework for the standardized classification of morphologic differences between craterforms. The shapes of paterae on Io are compared with calderas on Mars, lunar impact craters, and terrestrial ash-flow calderas and basaltic shield volcanoes. We used the criteria of Pike and Clow (1981) as modified by Radebaugh and Christiansen (1999) to classify the terrestrial volcanoes examined. The objective of this study is to determine if patterns in craterform shapes can be quantitatively identified using outline-based shape analysis, thus evaluating whether morphologic patterns have the potential to provide information about the formation of surface landforms.

2 BACKGROUND

2.1 Shape in the Natural Sciences

Shape is inherently subjective to human visual perception, and its interpretation is inclusive to personal experiences and prior knowledge, in conjunction with psychological, cultural, and ocular influences (Neal and Russ, 2012; Bookstein, 2014; Lestrel, 2015). The visual recognition and interpretation of shape is fundamental to human behavioral responses and few words in human language are able to effectively communicate detailed information about shape (Thompson, 1942; Lestrel, 2000). In particular, the recognition of objects by their outlines is fundamental to the human visual system (MacLeod, 1999; MacLeod, 2002). However, small structural details and subtle changes in closed contours are significantly less apparent (Lestrel, 2000; Loffler, 2008) but they can provide clues to extract geologic information. Unless differences can be readily identified in irregular outline data by the human visual system, fine distinctions can be dismissed when perception is inundated with nonconforming information (Lestrel, 2000).

Critical terms such as “morphometrics”, “shape”, and “size,” carry different connotative definitions in studies of form between the biological and geological sciences. Form, or morphology, describes size and shape (Fig. 2) and these properties communicate the fundamental principles of the physical, natural sciences: complexity, variability, and evolution. Complexity refers to the dissimilarity of the shape relative to the number of variables involved in the process

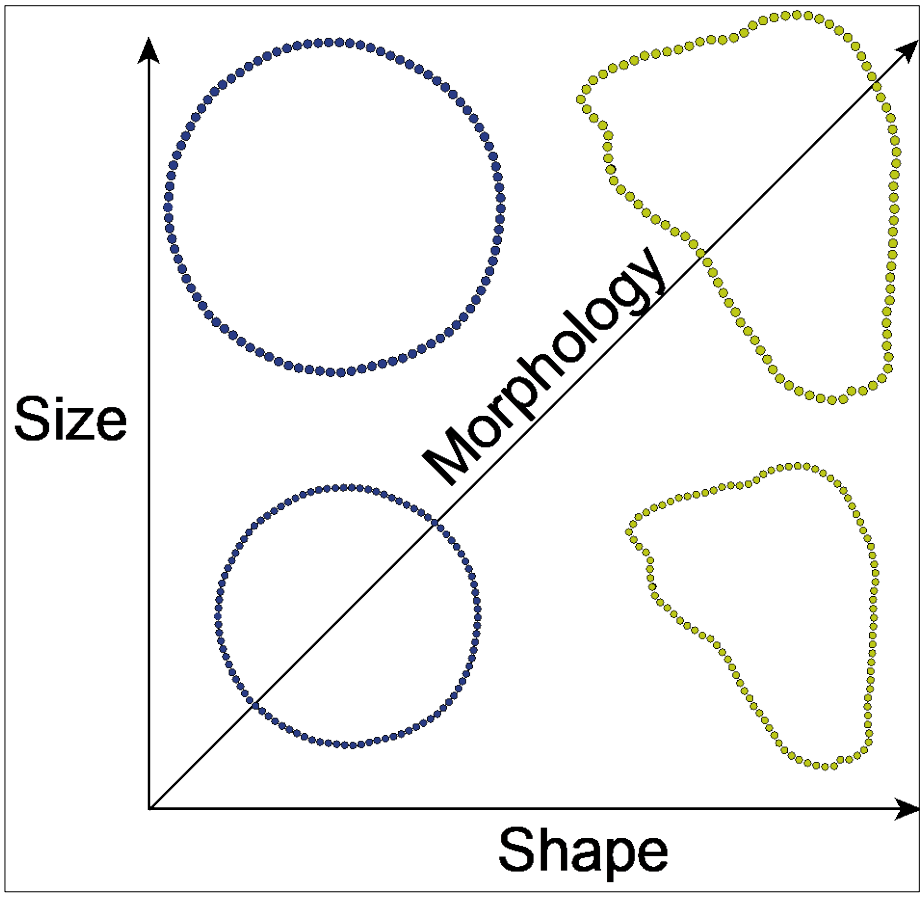

Figure 2 Form, or morphology, is a function of size and shape. Figure adapted from Richtsmeier et al. (2002).

(Lestrel, 2000). Variability refers to the differences in shape that are produced by a given process and is associated with the strength of certain formation mechanisms. Evolution refers to the change in morphology as a function of time (e.g., scarp collapse, volcanic resurgence, etc.) (Malin and Dzurisin, 1978; Mouginis-Mark and Rowland, 2001). While the morphologies of landforms on planetary surfaces provide rich visual information that enables scientific inferences to be made intuitively from comparisons with similar features, shape is not as easily quantified.

2.2 **Morphology and Morphometrics**

Morphology is an intrinsic property of all natural forms that provides the information used to interpret the systematic processes acting on the form over time (Greene, 1896). The concept of

form, or morphology, incorporating the properties of size and shape (Fig. 2), is elementary to the discipline of geomorphology (Evans, 1986; Lestrel, 1997). The ability to accurately classify craterforms is a fundamental task of planetary geology (Shoemaker, 1963; Greeley, 2011). Endogenic and exogenic planetary processes can produce craterforms similar in shape that yield opposing geologic implications for the evolution and age of planetary surfaces. Heavily impact cratered terrains suggest older surface ages and an inactive interior while the presence of volcanic craters and few (or no) impact craters suggest active resurfacing and thus an active interior. Identifying the differences in shape that are connected to the formation processes of craterforms will enhance our knowledge of the geologic history of planetary surfaces.

Landform shape is a fundamental aspect of geomorphology that is most effectively described using both qualitative and quantitative information (Huggett, 2016). Shape is defined in this study as the geometric properties of an outline, or closed contour, in two-dimensional plan view, invariant to translation, rotation, and size. The morphology of craterforms on planetary surfaces is controlled by many variables. Both endogenic (volcanic and collapse processes) and exogenic (impact cratering) mechanisms of crater formation fundamentally involve the transfer of energy through a geologic medium. Impact-induced crater morphology is dependent on the energy of the impacting bolide, the geophysical properties of the target body, and the physical properties of the impacting surface (e.g., Cintala et al., 1977; Wood et al., 1977; Grieve and Robertson, 1979; Pike, 1980; Ravine and Grieve, 1986). The morphology and shape of volcanic forms is dependent on three general groups of factors, including planetary variables, rheological properties of magma, and the intrinsic properties of eruption (Whitford-Stark, 1982; Greeley, 2013).

Morphologic information can be communicated multiple ways. The most common methods include semantic descriptions or classifications such as “circular”, “scalloped”, “rough”, “sharp”, or “angular” (Sayıncı et al., 2014). One example of this description method, the Powers (1953) sphericity -roundness classification system is a prominent example of how these descriptive classifications can be used to communicate powerful geomorphological information. Second, morphology can be communicated through measurements of internal dimensions and size from linear distances and ratios, using traditional morphometrics, also commonly referred to merely as morphometrics (Lestrel, 1997). Morphometrics is the measurement of shape and its dimensions (Marcus et al., 1996), and in context to geomorphology is explicated by Goudie (2003) as “the measurement of landforms”. The discipline of morphometrics consists of a number of procedures that quantitatively communicate measurement-derived information to enhance comparisons and relationships of morphology, or form (Read, 1990; Lestrel, 2015). Third, morphology can be examined by the analysis of shape using the bounding form of an outline (Lestrel, 1997) and its relative geometric properties that are invariant to scale, translation, and rotation using the mathematical technique of form comparison known as “geometric morphometrics” (Rohlf and Marcus, 1993). Figure 3 shows a flowchart of the various sub-disciplines of morphometrics and highlights the methodology used for this this study. This study uses boundary morphometrics techniques derived from the field of geometric morphometrics to examine the morphologic differences in forms lacking biological homology (Bookstein, 1998).

The ability of quantities, or shape descriptors, to communicate specific aspects of relevant information is dependent on the complexity of the posed hypothesis and extent of morphologic differences among the compared forms (Lestrel, 2000). The development of modern advances in the extraction of geologic information from observations could be greatly enhanced using

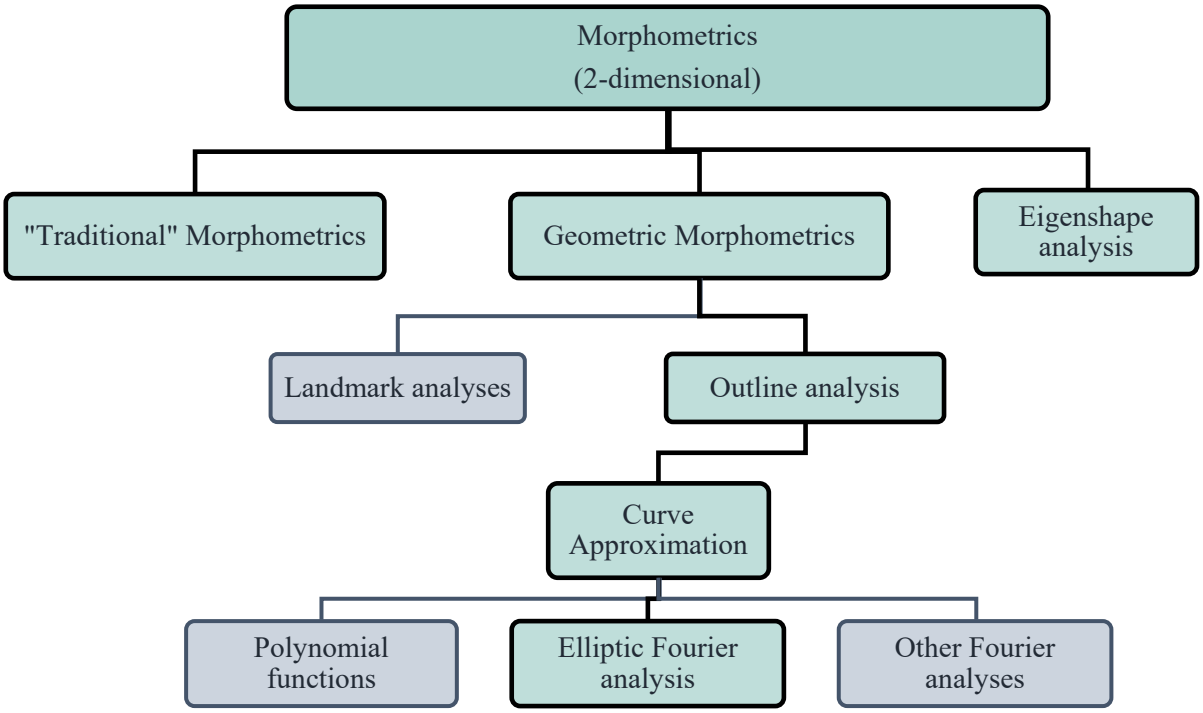

Figure 3 Flowchart of the sub-disciplines of morphometrics (Crampton, 1995); the methods used in this study are illustrated by the green boxes.

detailed quantitative comparisons of morphology. Traditional morphometrics and geometric morphometrics are both described in more detail below.

2.3 **Traditional Morphometrics**

Traditional morphometric methods can be useful to examine size and shape properties collected from physical measurements of natural forms (Lestrel, 1997). Commonly used morphometric measurements include length, width, perimeter, and area, as well as derived dimensionless ratios from these measures such as circularity, aspect ratio, best-fit ellipse, effective diameter, and others (Neal and Russ, 2012). While these quantities and ratios are easily calculated, significant shape information is lost and equivalent values can equally represent a range of different shapes. Traditional morphometrics provide quantities of shape that are not as effective for comparisons of complex forms (Evans, 1972; MacLeod, 1999; Sayıncı et al., 2014).

Furthermore, analyses of shape using these measures can yield morphometric results that fail to describe visually intuitive differences among the shapes in the analysis. Andrews-Hanna et al. (2008), for example, conclude that it is logically invalid to attribute patterns of ellipticity to endogenic geologic processes.

Modern craterform studies apply techniques of traditional morphometrics (Lohmann, 1983; Rohlf and Marcus, 1993; Lestrel, 2000) and directly link measurement-derived quantitative indices to geologic information and interpretations (e.g., Fassett et al., 2009; Michalski and Bleacher, 2013). These procedures use scalar measures such as area, perimeter, diameter, and depth, to compute values such as circularity (form factor), ellipticity, and depth-to-diameter ratio, which are used as primary quantitative descriptors of shape or form. These ratios are used to support interpretations and are most effectively applied where visual differences in morphology are substantiated a priori. However, these methods do not include the detailed spatial information specific to the geometry of a complex, or irregular outline or shape (MacLeod, 1999).

This study examines the morphology of paterae on Io, martian calderas, terrestrial basaltic shield calderas, terrestrial ash-flow calderas, and lunar impact craters using quantitative, outline-based shape analysis and multivariate statistical methods to evaluate if morphologic distinctions can be classified using shape information alone.

2.4 **Geometric Morphometrics**

Geometric morphometrics (Rohlf and Marcus, 1993) is a field of study pertaining to a set of methods that express shape quantitatively and preserve all geometric information throughout statistical analysis, while allowing shapes to be reconstructed to their original form. Geometric

morphometrics has 30+ years of legacy in fields of biological research (MacLeod, 2017a), and its results can address a larger number of scientific problems by communicating detailed quantitative comparisons of shape effectively. Shapes are examined by techniques that disregard variables including scale, translation, and rotation (Slice, 1996) and use procedures that enable visually intuitive comparisons of shape in an analytically tractable manner (MacLeod, 2002). By examining the correlations among the shapes of different populations of craterforms, formation processes can be extracted. Outline-based, "landmark-free" (does not depend on location) methods of shape analysis, descending from the advent of geometric morphometrics known as "boundary morphometrics" (Lestrel, 1997), are used to investigate patterns in the geomorphology of the craterforms examined in this study.

Studies using geometric morphometrics are accomplished by removing all non-shape variation (scaling, translation, and rotation) prior to quantitative analysis to allow shape information to be extracted for further analysis (Adams et al., 2013). Non-shape variations result from location and scaling of each craterform in the image (see Fig. 4). The outline is traced and

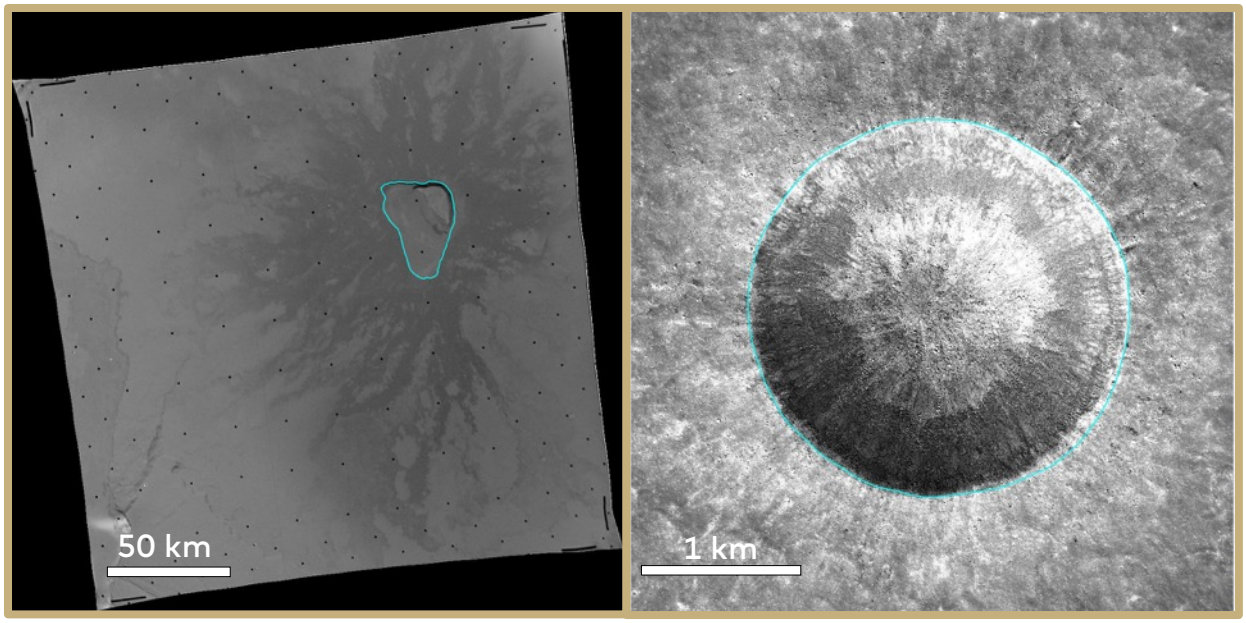

Figure 4 Non-shape variables of position, translation, and scaling result in differences in craterform location within processed imagery.

Cartesian coordinates are then extracted (see Fig. 6). One standalone method standard in geometric morphometrics to accomplish this is Procrustes analysis. However, this technique poses issues for the analysis of geomorphologic information as it assumes at least one (topologically) homologous point exists, from which procedures for standardized rotation among all forms can be accomplished. Craterforms of different origins inherently lack any such homology and thus this method produces erroneous results for craterforms. This presents a significant problem to "landmark-free" outline analysis studies as the quantities derived from each outline must be ordinal to some mark of reference. Ergo, mathematically-derived starting points along each outline, known as artificial, geometric, or "pseudo"-homologous points (Sneath and Sokal, 1982; O'Higgens, 1997) or Type III landmarks (MacLeod, 2011a) are derived for the craterforms by rotating the shapes to the point corresponding to the maximum distance from each shape's centroid. This study employs other methods that are able to manage the non-homology inherent to craterforms in comparison to Procrustes analysis.

2.5 **Previous Outline Studies of Morphology in the Geological Sciences**

The scope of application for geometric morphometrics has been thus far limited to studies of forms in the natural sciences because variability is intrinsic to the natural world. Difficulties in the description of form exist for both biological and geological specimens. While the biological sciences community has developed the field of geometric morphometrics to address the difficulties that arise in describing biological form (Lestrel, 1997), the modern geological sciences community has yet to take advantage of this methodology.

Pioneering studies in the analysis of grain shapes by Ehrlich and Weinberg (1970) introduced outline-based analysis approaches to the geological sciences community through

Fourier analysis as an "exact" method to characterize grain shapes. The Fourier series expansion can be used to quantitatively examine shapes treated as closed curve periodic functions by providing an approximation to the curve using any infinite number of harmonics to derive frequencies and amplitudes. The application of traditional, radial Fourier analysis to examine the variability among simple closed curves derived from the outline of geologic forms has been applied to lunar impact craters by Eppler et al. (1977a; 1977b; 1978; 1983), and Ravine and Grieve (1986) to examine the variability in, and to identify influential factors affecting, morphology in lunar craters. Additional applications of Fourier analysis in other planetary studies include Kordesh et al. (1982), Kordesh and Basu (1982), Kordesh et al. (1983), Kordesh (1983a); Kordesh (1983b), to analyze the differences between lunar soil particle shapes and clasts in meteoritic breccia.

The results of these studies were limited to the availability of multi-dimensional data reduction procedures and subsequent robust statistical methods of comparison enabled by advances in computational power and the maturation of outline-based shape methods. Eppler et al. (1978) and Eppler et al. (1983), employ the "closed form" method of Fourier analysis from Ehrlich and Weinberg (1970) which assumes some number of k points are placed at equiangular intervals originating from the shape's centroid.

In these analyses, the shape's centroid is calculated from all of the points initially placed along the outline; however, the centroid of the k points placed at equal angle intervals differs from the absolute centroid of the shape, and this introduces significant error into subsequent Fourier analysis because the assumption of equiangularity is violated (Ehrlich et al., 1983; MacLeod, 2011b). Furthermore, these results are limited in their scope of geological interpretation by proxy in identifying combinations of statistically significant harmonic

frequencies and amplitudes. The interpretations of these studies relied on comparisons of the presence of patterns among individual statistically significant Fourier descriptors produced from analysis. Ultimately the conclusions of these outline-based studies were limited by available multivariate statistical analysis and computational power, as well failing to reconcile a standard procedure for the requisition of the inherent flaws in these analyses pointed out by Ehrlich et al. (1983) and others. Studies of geomorphological forms using Fourier-based analysis largely died out in the late 1980's following the failure to resolve the discrepancies. A more recent application of radial Fourier analysis to craterforms by Watters et al. (2017) did not follow the methods used by the biological community that we pursue here.

While some recent studies have explored quantitative frameworks to standardize lunar crater classifications using methods such as the application of Chebyshev polynomials (e.g., Mahanti et al., 2014), these methods rely upon high-resolution topographic data. The use of polynomials (e.g., Craddock and Howard, 2000) and power laws (e.g., Baldwin, 1963; Pike, 1977) have been used to describe certain aspects of morphologic relationships for selected crater populations. The mathematical representation of craterform morphology using outline shape information has yet to be examined using modern multivariate approaches on any planetary body.

3 METHODOLOGY

3.1 Image Sources and Outline Digitization

We examined the shapes of 406 craterforms consisting of identified paterae on Io, lunar impact craters, martian calderas, and terrestrial basaltic shield calderas and ash-flow calderas. We use a stereographic map projection applied to each image from which outlines were obtained. A stereographic map projection ensures conformality (shape preservation) is preserved in contrast to other map projections that compromise shape distortion for correct scaling. The images in Appendix A are projected in stereographic map projection with *ad hoc* procedures implemented to correct the scale bars of each image. An example of the distortions in shape and scale that occur as a result of different map projections is illustrated in Fig. 5.

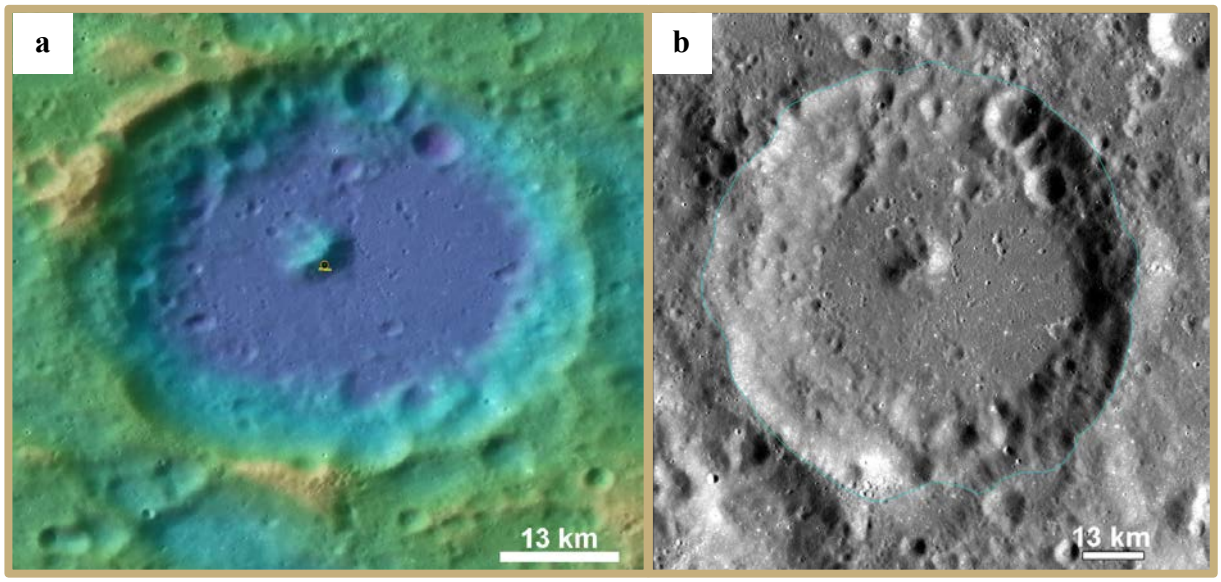

Figure 5 (a) Rheita crater on a shaded relief map using an equidistant cylindrical projection and (b) Rheita crater using a stereographic map projection of LROC WAC imagery. Image credit: lroc.sese.asu.edu, (a) 100 m/px LROC DEM; (b) 100 m/px LROC WAC.

3.1.1 Sources of Images

First, lists of craterforms produced by different processes were generated for different groups of craterforms. A sample consisting of 154 paterae on Io with well-defined boundaries and sufficient image resolution was examined in this study from images acquired by the *Galileo* Solid State Imaging camera (SSI) (Belton et al., 1992) and the *Voyager 1* Narrow Angle Camera (NAC) (Smith et al., 1977), retrieved from the Planetary Data Service (PDS), and processed in the ISIS3 software developed by the U.S. Geological Survey (https://isis.astrogeology.usgs.gov). The spatial resolution of the imagery used ranges from ~7 m/px to ~2 km/px, and since this is a sample dataset, not every patera at sufficient resolution was measured. The images of paterae were processed using Io 2000 IAU geographic datum and a polar stereographic map projection, with the central projection coordinates corresponding to the center of the image.

The Io *Galileo* SSI / *Voyager* Color Merged Global Mosaic base map provided by the U.S. Geological Survey Astrogeology Branch (Belton et al., 1992; Geissler et al., 1999; Becker and Geissler, 2005; Barth et al., 2009; Veeder et al., 2009; Williams et al., 2011b) was also used to collect observations of paterae at ~2 km/px spatial resolution. The mosaic was loaded into ESRI's ArcMap 10.4 software as a USGS *.cub* file using bilinear interpolation resampling using a stereographic projection coordinate system and the Io 2000 IAU geographic datum. The projected images of the paterae were exported as 2000 px by 2000 px .jpg files and included a scale bar (denoted in km (Appendix B)) that was later modified to correct for scaling errors introduced by the stereographic map projection for craters at high latitude.

Locations of terrestrial basaltic shield volcanoes and ash-flow calderas were taken from global databases provided by the *ASTER Volcano Archive* (AVA) and *Smithsonian Global Volcanism Program* (Venzke et al., 2002). Supplementary records and geologic mapping of ash-

flow shields are provided by Newhall and Dzurisin (1988), Lipman (1997), Radebaugh and Christiansen (1999), and Hughes and Mahood (2008). Images of a sample dataset of 38 ash-flow calderas and 35 basaltic shield calderas were collected in ArcGIS using ESRI's Online World Imagery base map layer and projected into a stereographic coordinate system. This base map layer contains imagery ranging in resolution from 15 m/pixel to the sub-meter scale depending on location. Where ESRI imagery was insufficient to resolve the complete shape) of the craterform due to image anomalies or obscuration from superficial effects such as clouds or snow, DigitalGlobe 2016® imagery ranging from ~1 – 15 m/px from Google Earth Pro (for n) was used. In some locations (for n), 30 m/px Landsat Enhanced Thematic Mapper (ETM) and 15 m/px Advanced Spaceborne Thermal Emission and Reflection Radiometer (ASTER) Visible and Near Infrared (VNIR) imagery from the USGS and NASA's Land Processes Distributed Active Archive Center (NASA LP DAAC 2015) were used.

Images of martian calderas documented by Hodges and Moore (1994), Williams et al. (2009), Robbins et al. (2011), and Tanaka et al. (2014) were taken from the THEMIS-IR Day Global Mosaic 100m v12 (Edwards et al., 2011) global image base map and CTX imagery using the JMARS software (Christensen et al., 2009). Martian calderas were located and the map was re-projected to the central coordinates of each caldera using the JMARS *Reproject....* tool to preserve conformal and equal-area attributes. The THEMIS IR Day v12 mosaic has a spatial resolution of 100 m/px; CTX imagery has a resolution of ~7 m/px and was used for some calderas (n) where higher resolution imagery was need to define their shapes. A sample of 24 calderas from Mars were studied.

Lunar impact craters were selected from the Lunar and Planetary Institute's Lunar Impact Crater Database (Losiak et al., 2015). The simple to complex transition causes morphologic

(shape) variation as the crater diameter increases. Simple craters are nearly circular, like bowls, and lack central peaks, while complex craters display more complicated morphologies and have central peaks, or pits. “Transitional” impact craters lack central peaks but have more complex rim outlines than simple impact craters. The simple to complex transition occurs at ~21 km for craters in the lunar highlands and at ~16 km diameter for craters in mare (Wilhelms et al., 1987). A simple random sample (SRS) of lunar craters was selected from the Lunar and Planetary Institute 2015 impact crater database (Losiak et al., 2015) binned by diameter ranges of [0-12 km], [12-35 km], and [35 – 220 km] to identify crater morphology associated with these ranges in size (Wilhelms et al., 1987). While the lunar simple-complex transition is related to size, but not defined by it, this method of sampling allows the diversity of impact craterform shapes on the Moon to be included in the study. Images of lunar impact craters were processed in ArcMap 10.4 from the LRO LOLA and Kaguya Terrain Camera DEM merge base map (Barker et al., 2016) and the LRO LROC-WAC Global Mosaic 100m June 2013 map. Similar to the other base maps, a polar stereographic map projection is used.

Craterforms with ambiguous origins were not used in this analysis. A total of 406 craterform outlines, consisting of 154 ionian paterae, 38 terrestrial ash-flow calderas, 35 terrestrial basaltic shields, 24 martian calderas, and 155 lunar impact craters were studied.

3.1.2 Outline Digitization

The tps series software (Rohlf, 2015) was used to digitize crater outlines from the selected images. This software stores data in the *tps* file format, the default file type used in geometric morphometrics software packages and scripts. A *tps* file is a simple text file that consists of a

series of Cartesian coordinates for a shape in a given image, with header lines that list additional information such as ID, image name, and scale factor.

Outlines were traced for each craterform manually by placing a number of points along the most continuous and well-defined outer boundary of the craterform using the *Curve* tool in *tpsDig2*. The initial point of each outline was arbitrarily placed in the northwest quadrant of the image along the structural bounds of the craterform followed by placement of points along the craterform rim in a clockwise fashion (Fig. 6a). Additional points can be placed until the outline satisfactorily represents the morphology of each craterform. The number of "raw" points needed to outline each craterform varies with the complexity of its shape. The final point on the curve is placed just before the initial point.

When all of the curves have been sufficiently outlined, the *tps* file was then modified in the *Sublime Text 3* text editor to complete the outline. A value of 1 was added to the value of points collected for each specimen, and the first listed Cartesian coordinate for each specimen is replicated onto the final line of its coordinates so as to geometrically close the shape of each of the outlined curves. Following these modifications, the file is re-opened in *tpsDig2* and the

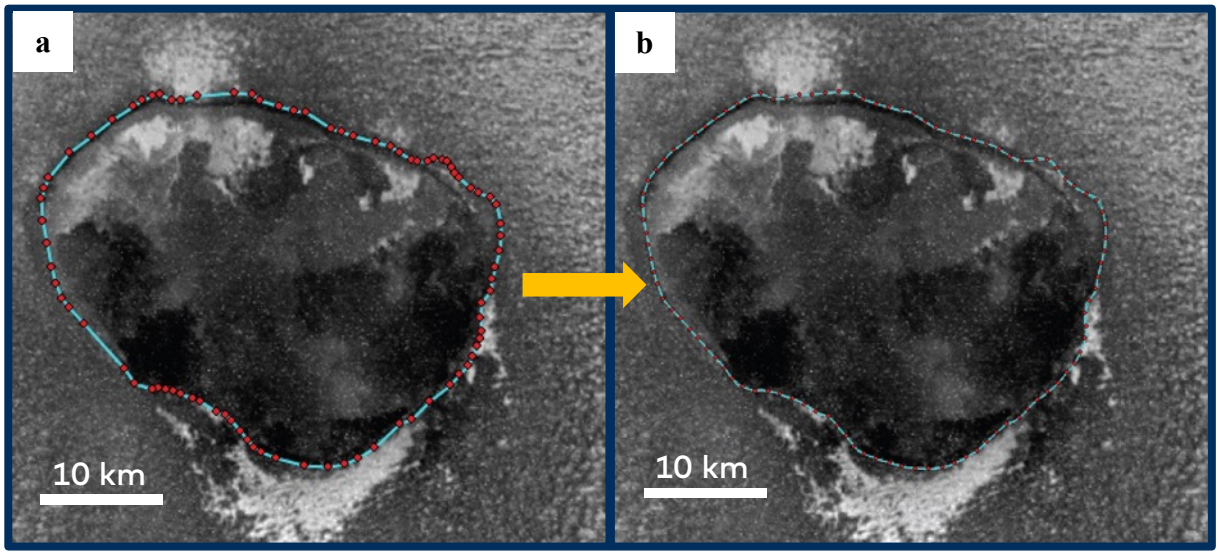

Figure 6 A visualization of the transformation from raw, maually placed Cartesian points (A) along the outline of the craterform to points with equidistant spacing (B) from linear interpolation.

outline is resampled to 100 equally spaced points using linear interpolation (Fig. 6b). The number of points is conventionally fixed at 99, consistent with other studies (Lohmann, 1983; Rohlf and Archie, 1984; Ferson et al., 1985). Interpolating the points to equal-length spacing ensures that the shapes can be compared at "positions of maximum correlation" (see Lohmann, 1983), since craterforms inherently lack topologically homologous landmarks. Mathematically derived, "pseudo-homologous" points (Sneath and Sokal, 1973) of reference were obtained for the shapes in the dataset by reordering the outline points to the point that corresponds with the maximum distance to the centroid.

After all of the craterform outlines have been resampled in tpsDig2, the relative area, perimeter, and circularity for each shape were calculated using the *tpsUtil* program. Following calculations of area and perimeter, the previously added point used to enclose each outline is removed since the quantitative methods employed assume the first and final point are connected. A total of 99 equally spaced points along each outline were collected and quantitative analysis was subsequently performed.

3.2 **Quantitative Analysis of Crater Shapes**

We employed multiple quantitative methods to examine and compare the craterforms and evaluate the ability of these quantitative analyses to describe the complexity and variability in shapes. Traditional morphometric measures of "circularity" (Eq. 1), also known as "formfactor" or "compactness," and "ellipticity," also known as "axial ratio," were calculated for each shape. Outline-based shape analysis methods, including the Zahn and Roskies (1972), or Z-R shape function, also known as the tangent angle approach, and elliptic Fourier analysis (EFA) were used to produce multivariate descriptors of the craterforms. Multivariate statistical methods

including principal component analysis (PCA) and discriminant analysis were then used to identify statistically significant differences between and among the groups of craterforms. This study tested the hypothesis that patterns between groups of craterforms can be quantitatively distinguished using quantities derived from outline-based shape analysis and multivariate statistical analysis.

3.3 Traditional Morphometrics: Circularity

Two-dimensional analyses derived from measurements of the morphology of landforms are often used in morphometric analysis of planetary surfaces. Circularity is defined by a shape's likeness to a circle in terms of its area and perimeter. The equation for circularity is:

$$Circularity = \frac{4\pi A}{P^2}, \quad (1)$$

where A is the area enclosed by a closed curve and P is the perimeter of the object. The result is a dimensionless quantity between 0 and 1, where a value of 1 indicates a circle and a value of 0 indicates a line between two points. For regular polygons, an equilateral triangle produces a circularity value of 0.61, a square yields a circularity value of 0.79, and the circularity of a pentagon is 0.87. Of course, circularity alone does not capture all of the geometric properties of shape. It is therefore preferable that multivariate methods of analysis are employed.

3.4 Multivariate Analysis: Z-R and EFA

Shape outlines can be quantified in multiple ways. A common approach is to fit a mathematical function to the sampled points of the outline in polar coordinates. A number of Fourier analyses can be applied to approximate a curve along the points of an outline, and the resultant coefficients from this approximation can then be subjected to multivariate analysis.

The Z-R shape function is an intuitive shape descriptor that is founded on the geometric properties of a circle, making it ideal to quantify impact and volcanic crater shapes. An analysis of boundary coordinates computed by the Z-R shape function results in a set of angles, expressed in radians, whose cumulative sum represents the angular change around the perimeter of the shape. The Z-R shape function is:

$$\phi(t) = \theta(t) - \theta(0) - t\,,$$

(***Error! Bookmark not defined.***2)

where t is the distance from the starting point, $\theta(0)$ is the tangent angle at the starting point, and $\theta(t)$ is the tangent angle of a vector of distance t from the starting point (Zahn and Roskies, 1972; Rohlf and Archie, 1984). The Zahn and Roskies (1972), or Z-R shape function (Eq. 2) evaluates the shape of an object by the curvature of its outline and provides an "intrinsic

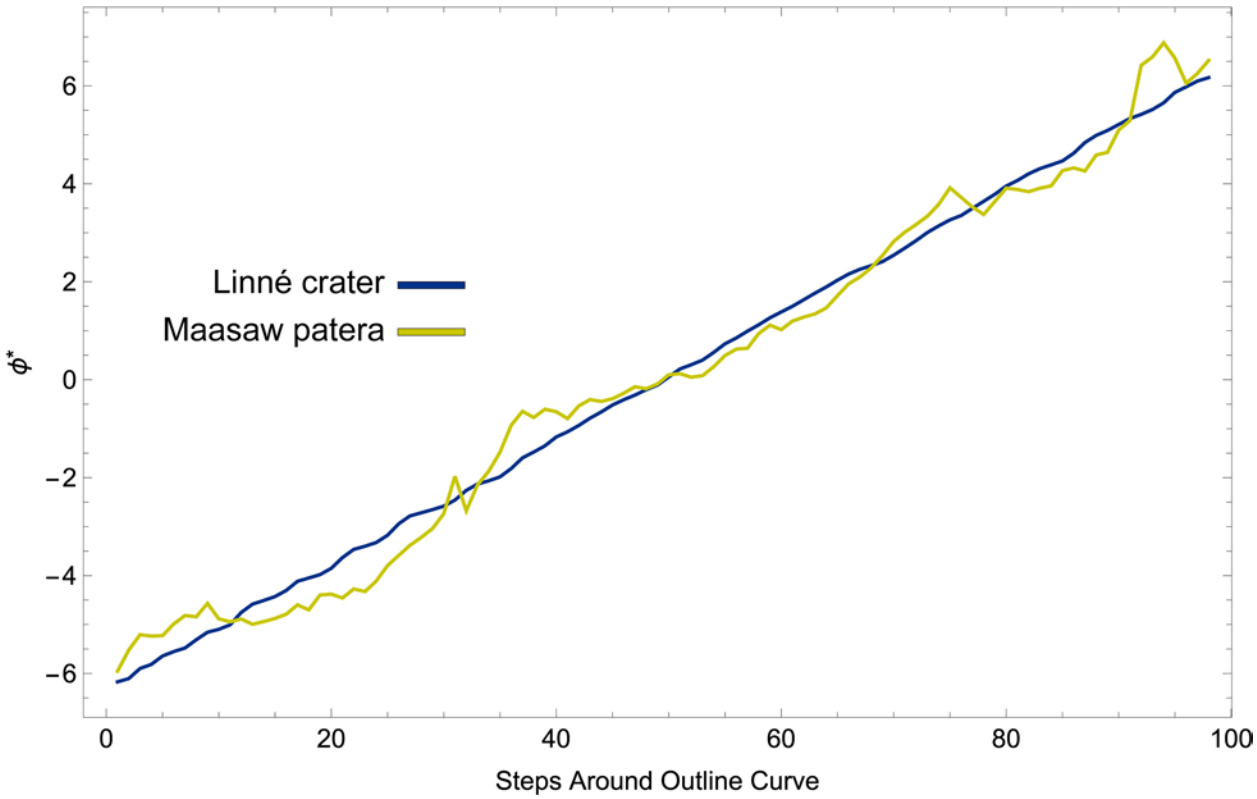

Figure 7 A plot of Z-R shape function results for Linné impact crater and Maasaw patera from their outlines shown in Fig. 4.

representation" of shape (Bookstein et al., 1982). The number of values output by the shape function correspond to the number of Cartesian points used to represent each outline. A total of

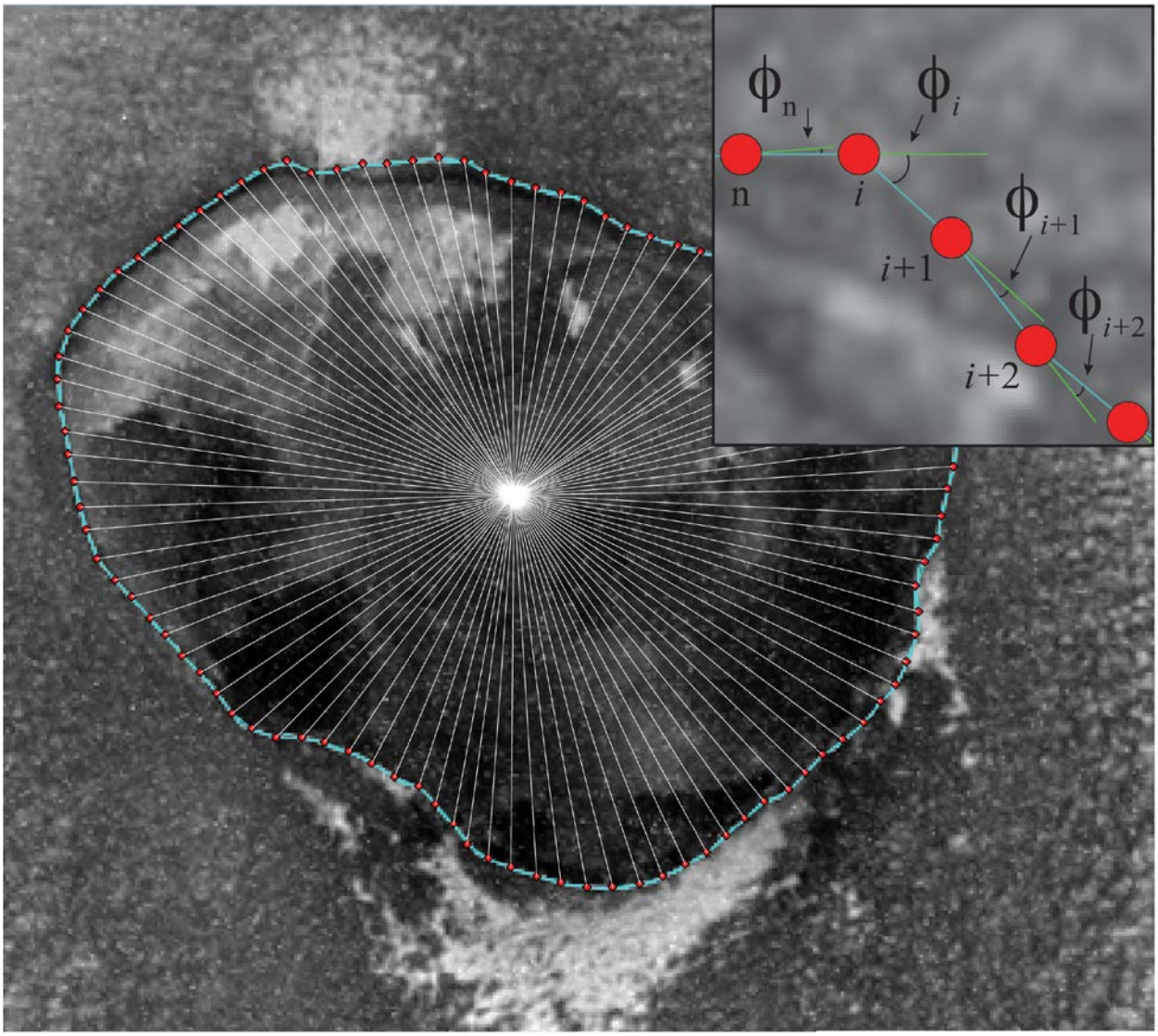

Figure 8 Z-R analysis of Camaxtli patera (Io), the ϕ-based approach, where (ϕ_i, ϕ_{i+1}, ϕ_{i+n}…) describes shape as the angular deviation from an ideal circular form.

98 output values are output from the function for each craterform and are collected into a matrix for further analysis. Figure 7 illustrates these quantities and their derivation along the outline of Camaxtli patera on Io.

Fourier analysis methods can also be applied to describe the change in tangent angle values of each point along the shape's curve as a function of arc length (Eq. 2). This "tangent angle approach" was proposed by Zahn and Roskies (1972) and the derived quantities were further subjected to Fourier analysis; however, others (Lohmann, 1983; Rohlf and Archie, 1984) took the raw quantities and realized that they could be examined alone to obtain similar results.

The Z-R shape function was applied using the *Wolfram Mathematica* software and MacLeod's (2011) "Z-R Shape Function 1.4" notebook (MacLeod, personal communication). Figure 8 shows a representation of Maasaw patera and Linné crater (see Fig. 1) according to Zahn and Roskies (1972) shape function. Linné crater is a nearly circular simple crater, and here plots as a nearly straight line while the more irregular Maasaw patera deviates from a circle. These measures are scale-invariant and isolate shape as a variable that can be quantitatively compared while allowing each shape to be easily reconstructed.

Elliptic Fourier analysis (Kuhl and Giardina, 1982), (EFA) is a widely-used technique of geometric morphometrics in outline analysis studies that provides a more precise approximation of complex shapes in comparison to traditional Fourier analysis and it is well-suited to boundary morphometrics (Rohlf and Archie, 1984; Lestrel, 2000). Elliptic Fourier analysis (Kuhl and Giardina, 1982) uses Fourier decomposition to separate the *x* (horizontal) and *y* (vertical) inter-point components of the outline as independent parametric functions of arc length and distance of each point from the starting point along the outline (Marcus et al., 1996; Lestrel, 1997, Kuhl and Giardina, 1982, Ferson et al., 1985; MacLeod, 2012).The parametric equations of the Z-R shape function, described by Kuhl and Giardina (1982) are:

$$x(t) = \sum_{n=1}^{N} \left[A_n \cos\left(\frac{2\pi nt}{T}\right) + B_n \sin\left(\frac{2\pi nt}{T}\right) \right], \quad (3)$$

$$y(t) = \sum_{n=1}^{N} \left[C_n \cos\left(\frac{2\pi nt}{T}\right) + D_n \sin\left(\frac{2\pi nt}{T}\right) \right], \quad (4)$$

where n equals the harmonic number, N equals the maximum harmonic number, t equals the incremental displacement between successive points along the outline, and T equals the total displacement over the complete shape.

The Fourier coefficients for *x* components of the shape function are (Kuhl and Giardina, 1982; Ferson et al., 1985):

$$A_n = \frac{\mathrm{T}}{2n^2\pi^2} + \sum_{p=1}^{k} \frac{\Delta x_p}{\Delta t_p} \left[\cos\left(\frac{2\pi nt_p}{T}\right) - \cos\left(\frac{2\pi nt_{p-1}}{T}\right) \right], \quad (5)$$

$$B_n = \frac{\mathrm{T}}{2n^2\pi^2} + \sum_{p=1}^{k} \frac{\Delta x_p}{\Delta t_p} \left[\sin\left(\frac{2\pi nt_p}{T}\right) - \sin\left(\frac{2\pi nt_{p-1}}{T}\right) \right], \quad (6)$$

where k is the number of steps in the trace (indexed by p), Δx_p is the displacement along the x-axis of the outline between steps $p-1$ and p, Δt_p is the length of the linear segment between these steps, t_p is the accumulated length of such segments at step p, and T (=t_k) is the total length of the closed curve. Similarly, the Fourier coefficients for the *y*-aspect are:

$$C_n = \frac{\mathrm{T}}{2n^2\pi^2} + \sum_{p=1}^{k} \frac{\Delta y_p}{\Delta t_p} \left[\cos\left(\frac{2\pi nt_p}{T}\right) - \cos\left(\frac{2\pi nt_{p-1}}{T}\right) \right], \quad (7)$$

$$D_n = \frac{\mathrm{T}}{2n^2\pi^2} + \sum_{p=1}^{k} \frac{\Delta y_p}{\Delta t_p} \left[\sin\left(\frac{2\pi nt_p}{T}\right) - \sin\left(\frac{2\pi nt_{p-1}}{T}\right) \right], \quad (8)$$

These equations are used to compute the coefficients for a number of harmonics that are sufficient to quantitatively describe and compare the craterforms in this study. The resulting coefficients produce $\cos x$, $\sin x$, $\cos y$, and $\sin y$ coefficients for each *n* harmonic, which describe inter-point orientation independently in the horizontal and vertical direction and approximate the shape function. While the coefficients produced from the EFA procedure

defined by Kuhl and Giardina (1982) can be immediately subjected to multivariate statistical analysis, we use the normalization procedure of Ferson et al. (1985) to ensure the shape data is invariant to non-shape variables (scaling, translation, and rotation). While the application of various Fourier series expansion methods typically disregards these outline variables, the application of Fourier analysis to shape can be sensitive to rotation, scaling, and the starting point of the traced outline (Ferson et al., 1985). These variables can be normalized for the shapes in the study using the following matrix operations.

$$\begin{bmatrix} a_n & b_n \\ c_n & d_n \end{bmatrix} = \frac{1}{E^*} \begin{bmatrix} \cos\phi & \sin\phi \\ \sin\phi & \cos\phi \end{bmatrix} * \begin{bmatrix} A_n & B_n \\ C_n & D_n \end{bmatrix} * \begin{bmatrix} \cos n\theta & -\sin n\theta \\ \sin n\theta & \cos n\theta \end{bmatrix}, \tag{9}$$

where n is the harmonic of the computed set of Fourier coefficients. The size of the minor (semi-major) axis, E^*, of the best-fit ellipse and the angular orientation of the ellipse ϕ expressed in radians are given by:

$$E^* = \sqrt{a^{*2} + c^{*2}} \tag{10}$$

$$\phi = \sin^{-1}\left(c^*/a^*\right) \tag{11}$$

on the interval $0 \leq \phi \leq 2\pi$. Normalized coefficients, $a^*$and c^* are given by the equations:

$$a^* = A_1 \cos\theta + B_1 \sin\theta, \tag{12}$$

$$c^* = C_1 \cos\theta + D_1 \sin\theta. \tag{13}$$

The calculation of θ is given by:

$$\theta = \frac{1}{2}\tan^{-1}\left[\left(2\frac{(A_1B_1 + C_1D_1)}{{A_1}^2 + {C_1}^2 - {B_1}^2 - {D_1}^2}\right)\right] \tag{14}$$

on the interval, $0 \leq \theta < \pi$.

As a result of this normalization procedure, the first three coefficients of the first harmonic, $\cos x_1$, $\sin x_1$, and $\cos x_1$ (a^*, b^*, and c^*) are degenerated to values of 1, 0, and 0 respectively and thus yield values that are not useful in further statistical analysis. The fourth coefficient of the 1st harmonic, $\sin y_1$ (d^*), however, provides the ellipticity (also known as axial ratio) of the best fit ellipse for each shape, and thus contributes meaningful shape information. Successive harmonics yield additional coefficients that produce a function that fits the outline of a shape with increasing precision.

It is desirable to limit the number of coefficients to the lowest number of harmonics necessary to adequately represent the shape differences among the craterforms. Similar to all other Fourier analyses, the first few consecutive harmonics (following the 1st) provide most of the information needed to approximate the shape.

The number of harmonics necessary to adequately describe the complexity across all of the craterforms was evaluated *a posteriori* in multiple ways. One way, shown in Fig. 9, is to visually examine successive harmonic shape approximations in comparison to the original outlines to determine how many harmonics are sufficient to represent the complexity of craterforms included in the study (Crampton, 1995). Another example of this is shown by Fig. 10 applied to

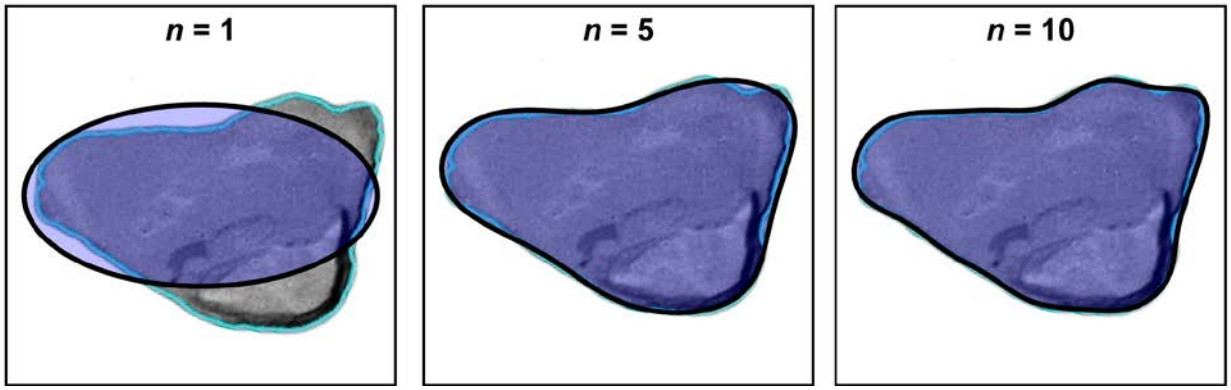

Figure 9 An example of elliptic Fourier analysis applied to the shape of Maasaw patera. As successive harmonics are applied, a better approximation of shape results at the cost of the inclusion of additional coefficients in the dataset.

the global computed values of the Fourier power (for the first 30 harmonics. The PAST3 (PAleontological STatistics) software package (Hammer et al., 2001) was used to compute the normalized elliptic Fourier analysis coefficients with the implementation of the Ferson et al. (1985) normalization procedure. From *a posteriori* examinations, we select the first 5 harmonics and 10 harmonics as adequate descriptors of the complexity and variability of the shapes included in this study. The coefficients corresponding to these harmonics were included in the multivariate statistical analysis in order to compare the differences and ability of the two quantitative descriptors to differentiate and successfully classify craterforms by shape alone. Due to the degeneration of the first three coefficients of the first harmonic due to the Ferson et al. (1985) normalization, and considering the final coefficient of the first harmonic represents ellipticity, which is extracted to be examined separately, the first harmonic is effectively removed and the number of coefficients as a function of its harmonic is $4n - 4$. Thus, we subject 16 coefficients (n=5) and 36 (n=10) coefficients from elliptic Fourier analysis to multivariate

analysis to determine the model that most accurately assigns membership of craterforms to their groups identified *a priori* (achieves the highest rate of success in classification) in this study.

3.5 **Outlier Identification Criteria**

Analysis of the shape quantities for each craterform produced by elliptic Fourier analysis and the Z-R shape function was completed using the *PAST3* (Hammer et al., 2001) and *JMP 13 Pro* (SAS Institute Inc., 2017) statistical software packages. Univariate statistical tests were computed to test the statistical significance (α=0.05) of diameter, circularity, and ellipticity using analysis of variance (ANOVA), while multivariate analysis of variance (MANOVA) tests were used to examine the multivariate dataset (elliptic Fourier coefficients. Z-R shape function angles). Multivariate outlier analyses (pooled within-group) were conducted for each group of craterforms using tests to examine Mahalanobis Distances, Jackknife Distances, and T^2 values in

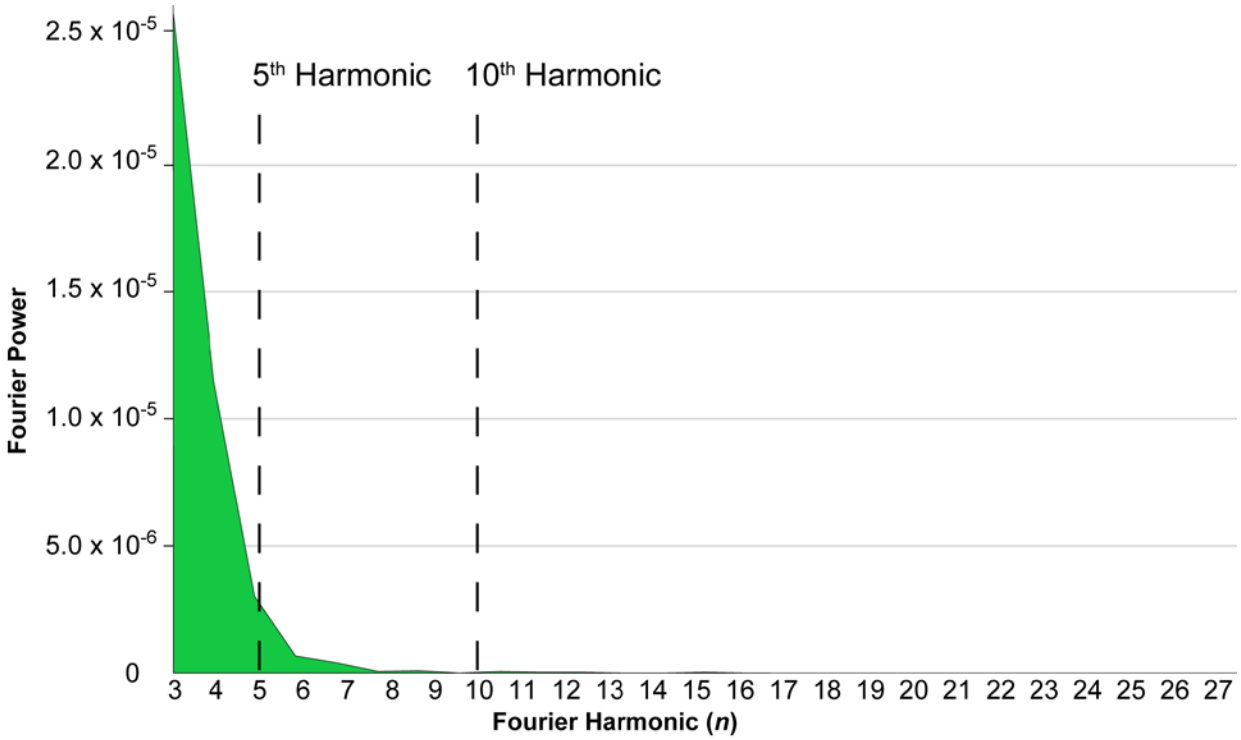

Figure 10 The averaged Fourier power values for each harmonic of elliptic Fourier analysis of all craterforms. The plot shows how contributed shape information, the area under the curve, changes as the harmonic number increases. The power values for the 1st and 2nd harmonics are excluded from the plot and are 1.82E-04 and 6.23E-04, respectively.

JMP *13 Pro*. The craterform groups were assumed to have unequal variances. In all analyses, a confidence coefficient of $\alpha = 0.05$ is implemented and 95% confidence ellipses are used to visualize relationships between groups. No craterform shapes were found to be outliers in this study defined by the criteria above.

3.6 **Multivariate Statistical Analyses**

Multivariate statistical analyses allow multiple variables to be examined simultaneously for an individual among a larger population. Reducing the many dimensions of the data that describe a single shape is critical in this process. To correlate the data, we used a variant of discriminant analysis known as canonical variate analysis (CVA). We subjected the 98 angular values for each craterform shape, computed from the Z-R shape function and the harmonic coefficients from elliptic Fourier analysis (for 5 and 10 harmonics, in separate runs) to separate multivariate statistical analyses, including discriminant analysis and principal component analysis. Both techniques reduce the dimensionality of the dataset to show the greatest amount of shape information in a 2-dimensional space. As any single column of variables for the craterforms can be compared against all others in a dataset, the dimensionality of a multivariate dataset is p-1.

A confidence level of 95% ($\alpha = 0.05$) is used to conclude that the true mean of a group lies within the range of values represented by its ellipse. Significance is considered using an *ad hoc* procedure examining the resultant p-values from statistical analysis in context to others produced. A p-value describes the likelihood of the statistical result to be replicable from random data and correlates directly to the selected α level of confidence. As this study employs

exploratory methods, *p*-values are examined comparatively and within reason, and thus statistical significance is not limited in absolute to *p*-values > 0.05.

3.7 **Principal Component Analysis**

Principal component analysis (PCA) is a form of multivariate statistical analysis that seeks to maximize the variance of a linear combination of variables and, in this study, provides a visually intuitive way to interpret shape differences in craterforms. The objective of this method is to represent maximum variability in the data using the fewest number of components. It allows proportions of variance among the total population to be explained by the principal dimensions of variation within a dataset. Principal component analysis is often used as a data-dimensionality reduction technique that allows sets of many variables, such as the 98 angular values produced for each shape by the Z-R shape function, or the 36 elliptic Fourier coefficients of the 10^{th} harmonic produced by the EFA procedure, to be visualized using principal axes of variance in a two-dimensional space. Data dimensionality reduction in PCA is achieved by eigenanalysis, a procedure of finding the eigenvalues and eigenvectors of the correlation matrix using the Singular Value Decomposition (SVD) algorithm. The computed eigenvalues provide a measure of variance among the data corresponding from the eigenvectors (principal components) usually represented as the axes of a 2D plot. The application of PCA to the output of the Z-R shape function is known as "eigenshape analysis" (Lohmann, 1983; Lohmann and Schweitzer, 1990).

3.8 **Discriminant Analysis (Canonical Variate Analysis)**

Discriminant analysis is a form of multivariate analysis that examines and maximizes the differences between groups distinguished *a priori* from a population while minimizing within-group variation for one or more classification criteria. The two fundamental objectives of

discriminant analysis are first, to optimally describe group separation and second, to predict where measurements will fall into groups using a classification function (Rencher and Christensen, 2012). The first task is known as “canonical discriminant analysis” whereas the second task is referred to as “classification analysis” or “supervised classification”. Canonical variate analysis (Fisher, 1936), or CVA, is a type of discriminant analysis that is intended to maximize the differences between multiple groups (k >2) in a population (Lestrel, 2000). This analysis performs a series of standardized axis rotations and transformations, which result in the data for the two or more groups to optimally project onto a lower dimensional space where maximum differences between the mean value of each group can be visualized. The first canonical variable represents the linear combination of the coefficients that maximizes the multiple correlation between the craterform groups and the coefficients. The second canonical variable is a multiple linear combination, mathematically independent to the first, that maximizes correlation between the craterform groups (SAS Institute Inc., 2017). Discriminant analysis is useful to identify the specific variables that contribute to group separation. It is used in this study to provide the framework of a classification system by which additional (unknown) craterform shapes lacking *a priori* classification could be assigned to a specific group based on multiple quantities of form, including shape-derived quantities.

Discriminant analysis was completed with the JMP 13 Pro software using the Z-R shape function and the coefficients produced from elliptic Fourier analysis. The quadratic method of discriminant analysis was chosen because the covariance matrices of the shape quantities for the craterform groups are unequal and it is particularly robust to within-group differences between covariance matrices for the craterform populations (Friedman, 1989). It also provides a better fit of the classification function to the data in this study in comparison to linear fits.

4 RESULTS

4.1 Diameter

Diameter values for the craterforms are displayed in Figure 11 and summarized in Table 1. Figure 11 shows outlier box plots for each group where the boxes represent the interquartile range (IQR), derived by subtracting the 3rd quartile from the 1st quartile; the line within the box represents the group mean. The "whiskers" or lines extending from each box, are drawn to the

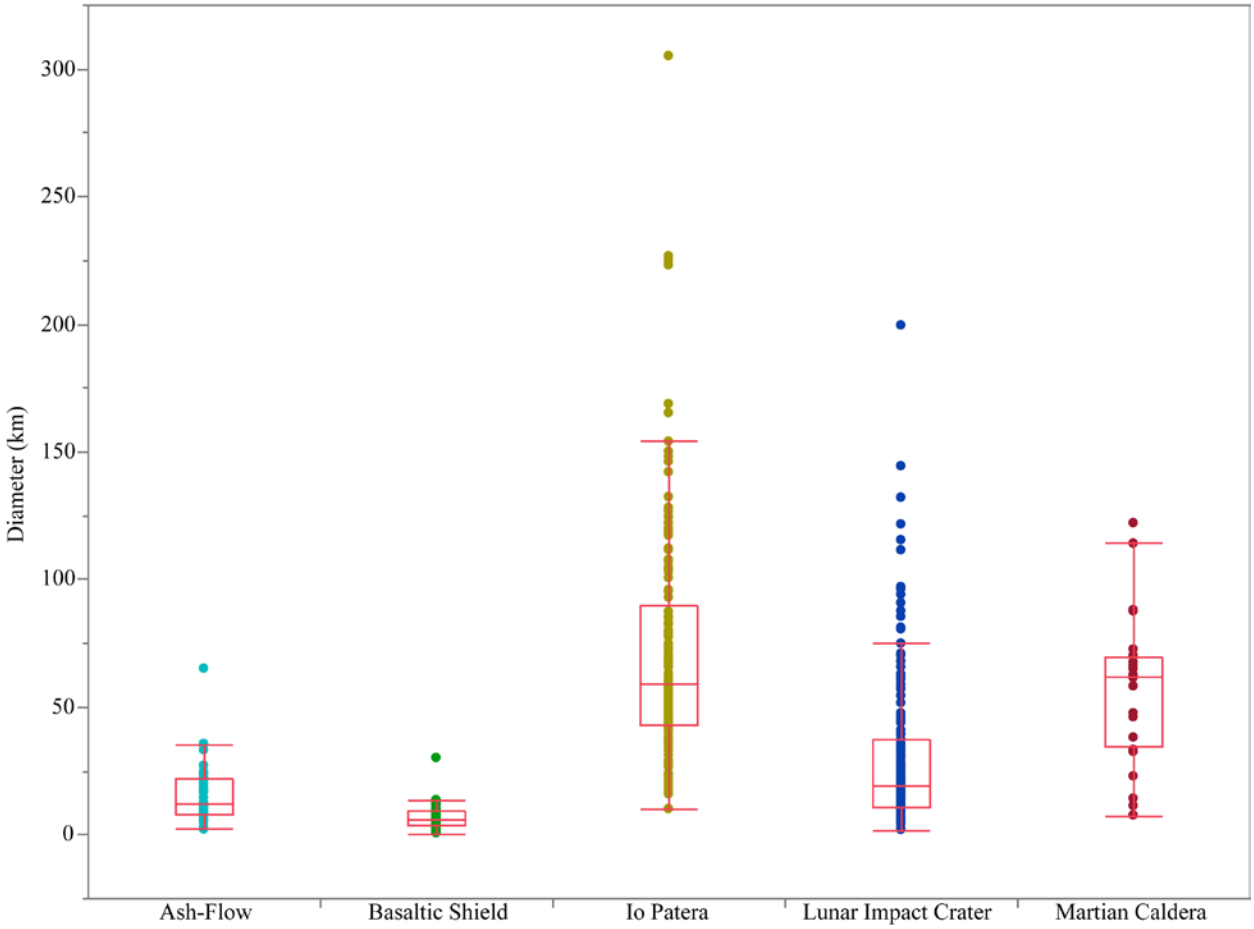

Figure 11 Diameter box plots and values for the craterforms examined in this study.

Table 1 Crateriform group diameter means and standard deviations in km.

Level	Number	Mean	Std Dev	Lower 95%	Upper 95%
Ash-Flow	38	16.0	12.2	12.0	20.0
Basaltic Shield	35	6.8	5.3	5.0	8.6
Io Patera	141	71.9	45.6	64.3	79.5
Lunar Impact Crater	155	30.7	31.4	25.7	35.6
Martian Caldera	24	57.2	29.1	44.9	69.5

farthest point within the range of 1.5 times the IQR, points displayed beyond these lines represent potential outliers in terms of the IQR. Table 1 shows the mean diameters (km) for each group, the Lower 95% and Upper 95% represent the lower and upper limits of the confidence interval in the diameter values. While the measurement of diameter is inherently subjective in the determination of the major and minor axes of the craters, these values are taken from the literature (Newhall and Dzurisin, 1988; Radebaugh et al., 2001; Venzke et al., 2002) and from the *Gazetteer of Planetary Nomenclature*, courtesy of the IAU, USGS, and NASA (planetarynames.wr.usgs.gov).

As shown in Fig. 11 and Table 1, paterae on Io are the largest and most variable in size of the craterforms examined in this study, with a mean diameter of ~72 km +/- 45.6 km (1 standard deviation). Martian calderas are the second largest craterforms in this study with a mean diameter of ~57 km +/- 29 km. Lunar impact craters are the third largest craterforms in the study with a mean diameter of ~31 km+/- 31 km. It is important to reiterate that the lunar craters in this study were selected from a simple random sample that included an approximately equal number of simple craters, transitional craters, and complex craters. Based on crater-size frequency distributions (SFD), if the sample of lunar craters had been selected from the true global population of lunar craters, the mean diameter would be much lower (see Neukum et al., 1975), and the largest craterforms would have been lunar impact craters. Terrestrial calderas have the

smallest diameters with ash-flow calderas having a mean diameter of 16 km +/- 12.19 km and craters on basaltic shields having a mean diameter of 6.81 km +/- 5.28 km.

4.2 **Circularity**

Because we did not have accurately scaled values for area and perimeter, unscaled values from the shape measurements were used to calculate circularity for each craterform; since these are dimensionless ratios, they are size-independent. For any set of *n* digitized points, a true circularity value of 1 is impossible due to the presence of pixel values, inherent to all digital imagery. Considering that the points in this study are interpolated to 99 equidistant points, even an errorless outline of a circle can only be considered a regular 99-sided polygon with a mathematical maximum circularity value of 0.9997. Circularity distributions and values are summarized in Figure 11 and Table 2. Figure 12 shows an outlier box plot of circularity values. Table 2 shows the mean circularity for each group, their standard deviations, and upper and lower limits corresponding to 95% confidence intervals. This plot shows that most craterform groups have similar values of circularity but Io's paterae are the least circular. As expected, lunar impact craters are significantly more circular than any of the other examined craterforms with a mean circularity of 0.96 +/- 0.03 (1 standard deviation), also showing that lunar impact craters have the smallest variation in circularity. Martian calderas and terrestrial basaltic shield calderas are less circular than impact craters and have very similar mean circularities of 0.90 +/- 0.06 and 0.88 +/- 0.06 respectively. Moreover, they are more variable in circularity than impact craters. Ionian paterae (0.81 +/- 0.12) and ash-flow calderas (0.82 +/- 0.10) have nearly equivalent mean circularities and are significantly less circular than calderas on basaltic shields and martian

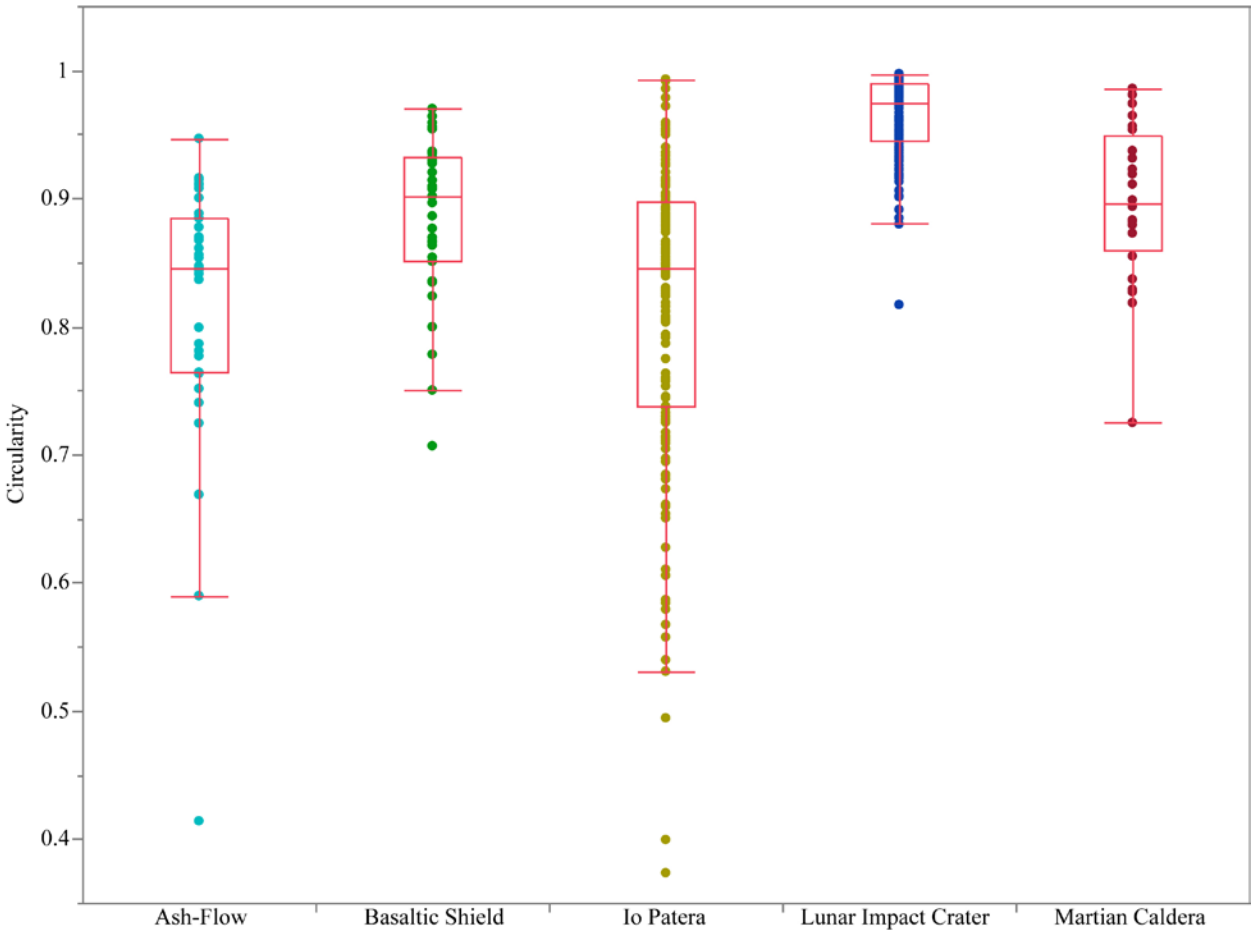

Figure 12 Box plots and plotted points of the circularity of the different classes of craters.

calderas. These two types of craters are also most variable in shape than the other categories as indicated by the large standard deviation (+/- 0.10-0.12).

Differences in circularity are subjected to paired statistical testing to examine what differences might exist between the groups from pairwise comparisons. Results from a non-parametric Tukey-Kramer test are shown in Table 3. A non-parametric Tukey test is chosen

Table 2 Statistics for craterform circularity.

Level	Number	Mean	Std Dev	Lower 95%	Upper 95%
Ash-Flow	38	0.82	0.10	0.78	0.85
Basaltic Shield	35	0.88	0.06	0.86	0.91
Io Patera	154	0.81	0.12	0.80	0.83
Lunar Impact Crater	155	0.96	0.03	0.96	0.97
Martian Caldera	24	0.90	0.06	0.87	0.92

Table 3 Results from a non-parametric Tukey-Kramer test of ellipticity. Statistically significant *p*-values are shown in orange and red and identify groups of craterforms that are different using group circularity values.

Level	- Level	Score Mean Diff	Std Err Diff	Z	p-Value
Lunar Impact Crater	Io Patera	133.98	10.17	13.18	<.0001*
Lunar Impact Crater	Ash-Flow	92.39	10.11	9.14	<.0001*
Lunar Impact Crater	Basaltic Shield	75.47	10.29	7.33	<.0001*
Martian Caldera	Io Patera	37.56	11.31	3.32	0.0080*
Basaltic Shield	Ash-Flow	16.44	4.97	3.31	0.0084*
Martian Caldera	Ash-Flow	16.28	4.7	3.46	0.0049*
Martian Caldera	Basaltic Shield	3.27	4.55	0.72	0.9526
Io Patera	Ash-Flow	2.15	10.07	0.21	0.9995
Io Patera	Basaltic Shield	-34.50	10.24	-3.37	0.0068*
Martian Caldera	Lunar Impact Crater	-62.36	11.37	-5.49	<.0001*

because the groups have non-equal variance, and a Tukey test is selected because a non-normal distribution is assumed for the craterforms within each group. Colored *p-values* shown in orange indicate statistical significance (a = 0.05) between the groups, orange indicates very small *p-values* while red indicate larger p-values, non-colored values indicate non-statistically significant results. The test shows that statistically significant differences exist between all paired comparisons except for paterae on Io and ash-flow calderas, and martian calderas and basaltic shield calderas.

4.3 **Ellipticity**

Ellipticity values for each crater, provided from the normalization procedure applied to the elliptic Fourier analysis, are shown in Figure 13 and summarized in Table 4. High ellipticity values indicate non-elongate shapes and low values indicate highly elongate shapes. While these measures are often derived from visual estimates of the major and semi-major axis, ellipticity in this study is derived from the first elliptic Fourier coefficient, $\sin y_1$ (d^*), a product of the shape normalization procedure of Ferson et al. (1985). While ellipticity values are conceptually similar

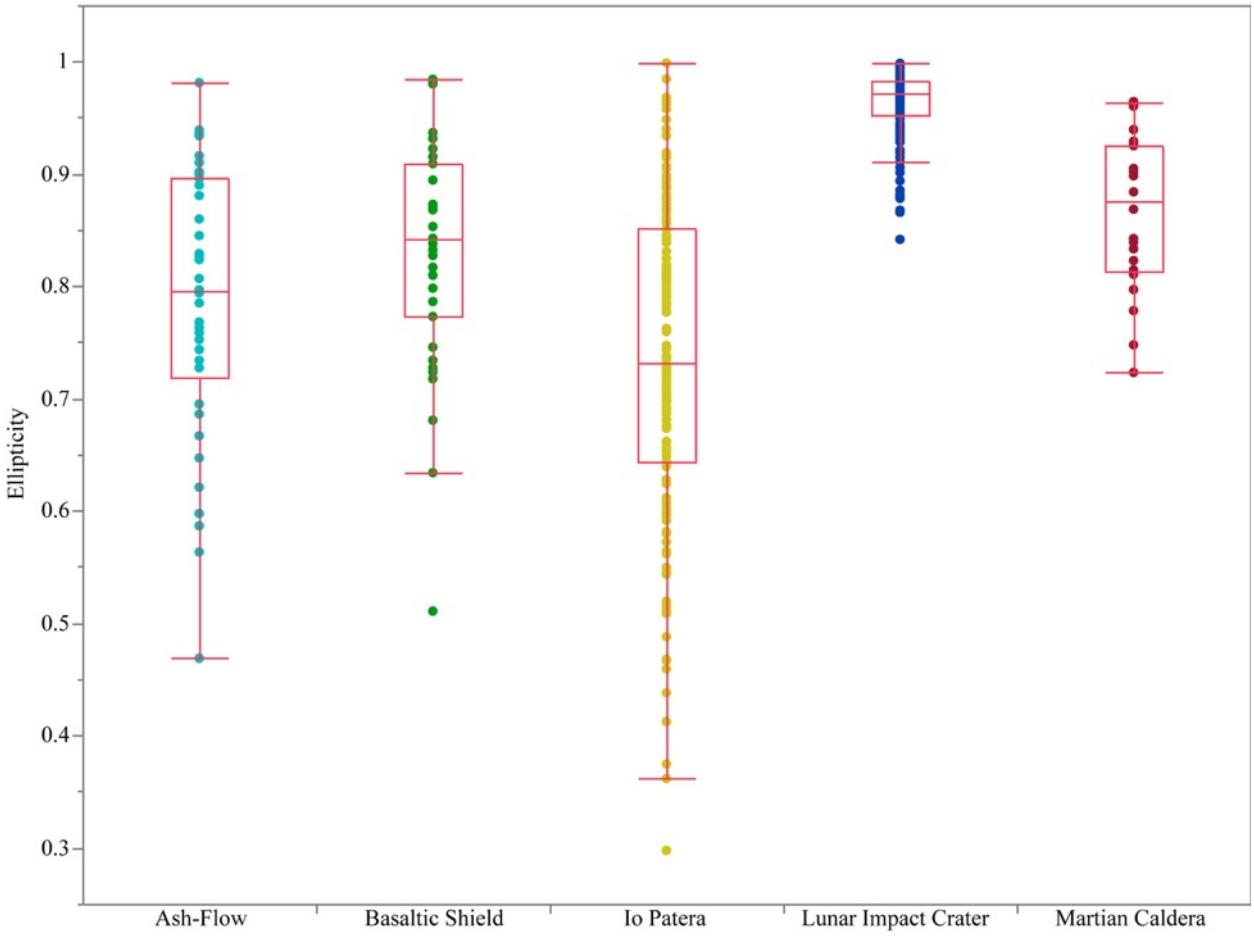

Figure 13 Box plots and plotted points for the ellipticity of the different classes of craters.

to circularity, they convey different information as they use internal shape properties of the principal horizontal and vertical axes of the shape. Ellipticity is equivalent in this sense to axial ratio, values close to 1 represent geometric similarity to a circle. They provide a best fitting ellipse using only using the information provided by the geometric placement of the coordinates

Table 4 Mean ellipticity, standard deviation, and confidence interval boundary values for the craterform groups.

Level	Number	Mean	Std Dev	Lower 95%	Upper 95%
Ash-Flow	38	0.79	0.12	0.75	0.83
Basaltic Shield	35	0.83	0.10	0.80	0.87
Io Patera	154	0.73	0.14	0.71	0.75
Lunar Impact Crater	155	0.96	0.03	0.96	0.97
Martian Caldera	24	0.87	0.07	0.84	0.89

for each shape, rather than using any information provided by area or perimeter, and furthermore eliminate any subjective influence in the determination of major and minor axes.

As expected, lunar impact craters have the higher ellipticity value than any of the other examined craterforms with a mean ellipticity of 0.96 +/- 0.03 (1 standard deviation), also indicating that lunar impact craters have the smallest variation in ellipticity. Martian calderas are more elliptical than impact craters with a mean ellipticity value of 0.87 +/- 0.07. As for circularity, calderas on terrestrial basaltic shields (0.83 +/- 0.10) and ash-flow calderas (0.79 +/- 0.12) are most similar among all of the groups in terms of their mean values and variations. Paterae on Io (0.73 +/- 0.14) have the lowest mean ellipticity value and highest standard deviation among all groups.

A non-parametric Tukey-Kramer test is applied to the univariate data to examine statistically significant differences between the ellipticity values of the groups and the results are shown in Table 5. The test shows that martian calderas and ash-flow calderas, basaltic shield calderas and ash-flow calderas, martian calderas and basaltic shield calderas, and ash-flow calderas and ionian paterae cannot by distinguished from one another with statistical

Table 5 Results from a non-parametric Tukey-Kramer test of ellipticity. Statistically significant *p*-values are shown in orange and identify groups of craterforms that are different using group ellipticity values.

Level	- Level	Score Mean Difference	p-Value
Lunar Impact Crater	Io Patera	143.74	<.0001*
Lunar Impact Crater	Ash-Flow	87.87	<.0001*
Lunar Impact Crater	Basaltic Shield	77.61	<.0001*
Martian Caldera	Io Patera	51.89	<.0001*
Martian Caldera	Ash-Flow	12.27	0.0688
Basaltic Shield	Ash-Flow	7.77	0.5217
Martian Caldera	Basaltic Shield	5.09	0.7967
Io Patera	Ash-Flow	-21.93	0.1876
Io Patera	Basaltic Shield	-39.40	0.0011*
Martian Caldera	Lunar Impact Crater	-75.09	<.0001*

significance. This result differs from the test on circularity values as it finds two additional group pairs of craterforms that are unable to be distinguished with statistical significance.

4.4 Discriminant analysis of EFA Coefficients from the 2nd to 5th Harmonics

The shapes of craterforms are next analyzed using multivariate statistical methods. Here we subject the elliptic Fourier coefficients of the 2nd to 5th harmonics, selected using *a posteriori* procedures (see Figure 9 and Figure 10) and produced by the elliptic Fourier analysis procedure for each craterform shape to discriminant analysis to examine the maximum differences between the groups. Figure 14 shows results from discriminant analysis of the first 16 elliptic Fourier coefficients (2nd to 5th EFA harmonics) for each craterform group. The ellipses shown in the plot represent 95% intervals of confidence that the group mean lies within the ellipse. The discriminant analysis is shown to be statistically significant by the statistical tests in Table 6 for

Table 6 Statistical significance test for discriminant analysis of the 2nd to 5th harmonic elliptic Fourier coefficients.

Test	Value	NumDF	Prob>F
Wilks' Lambda	0.415	64	<.0001*
Pillai's Trace	0.654	64	<.0001*
Hotelling-Lawley	1.249	64	<.0001*
Roy's Max Root	1.113	16	<.0001*

the null hypothesis. This shows that the means of the covariates are approximately equal across the groups of craterforms from discriminant analysis. The low p-values from the statistical tests indicate that the results of the analysis are statistically significant. Separation between confidence ellipses indicate significant differences between most craterform shapes. On the other hand, the 95% confidence limits for martian calderas and basaltic shield calderas largely overlap indicating that they have similar shapes.

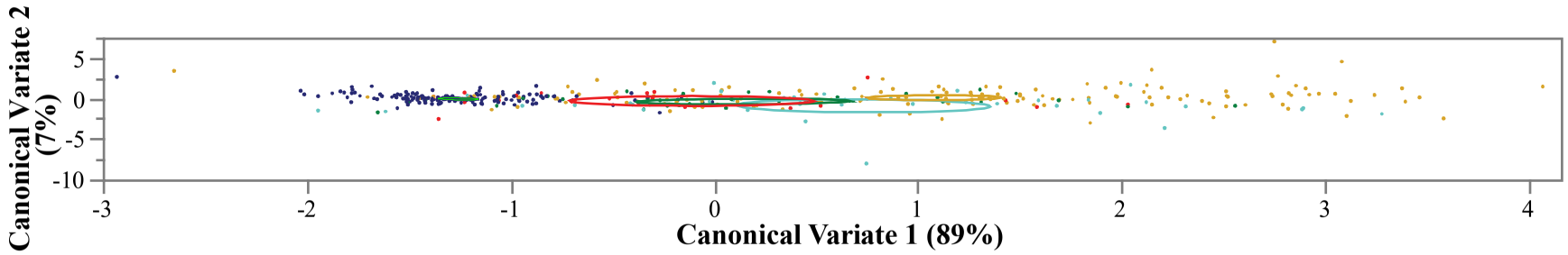

Figure 14 Canonical variate analysis results for the first 16 elliptic Fourier coefficients of the first 5 harmonics. The ellipse for lunar impact craters is highlighted in bright green.

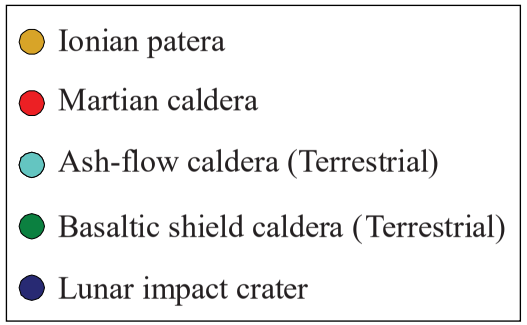

Table 7 shows that the first canonical variate is statistically significant and represents 89% of the total shape variance between the groups. Low *p-values* here indicate that the differences

Table 7 Statistical significance test for the 2nd to 5th harmonic canonical variates produced by discriminant analysis. The first canonical axis is shown in the first row and the additional axes follow sequentially.

Eigenvalue	Percent	Cum Percent	Canonical Corr	Likelihood Ratio	Prob>F
1.113	89.13	89.13	0.726	0.415	<.0001*
0.086	6.92	96.05	0.282	0.877	0.2231
0.031	2.52	98.57	0.175	0.952	0.8914
0.018	1.43	100	0.133	0.982	0.9026

between the groups of shapes, represented by the covariates, are statistically significant. The three other canonical variates account for residual differences in shape but each lack the power to statistically distinguish between groups. In this case, only the first canonical variate is statistically significant and thus the y-axis, or vertical displacement of the points shown in Figure 14 provides information that fails to sufficiently describe significant differences between the groups of shapes. To examine the information provided by the statistically significant first canonical variate, the canonical scores from this axis are extracted and plotted onto a density plot (Fig. 15).

Discriminant analysis is a powerful tool to examine the differences in the shapes of these crater types. Table 8 shows that using the assignments of craterform types known *a priori* and an estimation of the number of necessary harmonics from *a posteriori* assessment, the predictive model successfully assigns group membership to ~75.6% of the craterforms using the first 16

Table 8 Misclassification rate of predicted group assignments from the canonical variate analysis for the 2nd to 5h harmonics of EFA.

Source	Count	Number Misclassified	Percent Misclassified
Training	406	99	24.38

elliptic Fourier coefficients of the 2nd to 5th harmonics. Table 9 shows established classifications and predicted group membership from the canonical variate analysis, Table 10 shows the numbers iterated as percentages.

Table 9 Predicted group membership assignments produced by the canonical variate analysis of the elliptic Fourier coefficients from the 2nd to 5th harmonics.

EFA *n*=5	Predicted Count					
Group	**Ash-Flow**	**Basaltic Shield**	**Io Patera**	**Lunar Impact**	**Mars Caldera**	**Count**
Ash-Flow	26	4	5	0	3	38
Basaltic Shield	0	26	1	4	4	35
Io Patera	14	31	91	12	6	154
Lunar Impact	3	6	1	145	0	155
Mars Caldera	0	0	0	5	19	24

Table 10 Success rates for predicted group classifications based on shape from canonical variate analysis of the elliptic Fourier coefficients from the 2nd to 5th harmonics.

EFA *n*=5	Predicted Count					
Group	**Ash-Flow**	**Basaltic Shield**	**Io Patera**	**Lunar Impact**	**Mars Caldera**	**Count**
Ash-Flow	**68%**	11%	13%	0%	8%	100%
Basaltic Shield	0%	**74%**	3%	11%	11%	100%
Io Patera	9%	20%	**59%**	8%	4%	100%
Lunar Impact	2%	4%	1%	**94%**	0%	100%
Mars Caldera	0%	0%	0%	21%	**79%**	100%

The model successfully identifies group membership for 94% of the lunar impact craters included in the study while the other craterform groups show variation in the results of the model's prediction among more than one category. Of 154 total paterae, 91 (59%) are successfully assigned correct membership. Of the remaining paterae, 31 (20%) are assigned membership to the basaltic shield caldera group, 14 (9%) are assigned to the ash-flow caldera group, 12 (8%) are assigned to the impact crater group, and 6 (4%) are assigned to martian calderas. For the ash-flow caldera group, 26 of 38 (68%) are correctly assigned membership; 5 (13%) of ash-flow calderas are classified as paterae, 4 (11%) are assigned membership to the basaltic shield caldera group, and 3 (8%) are assigned classification to martian calderas. Basaltic

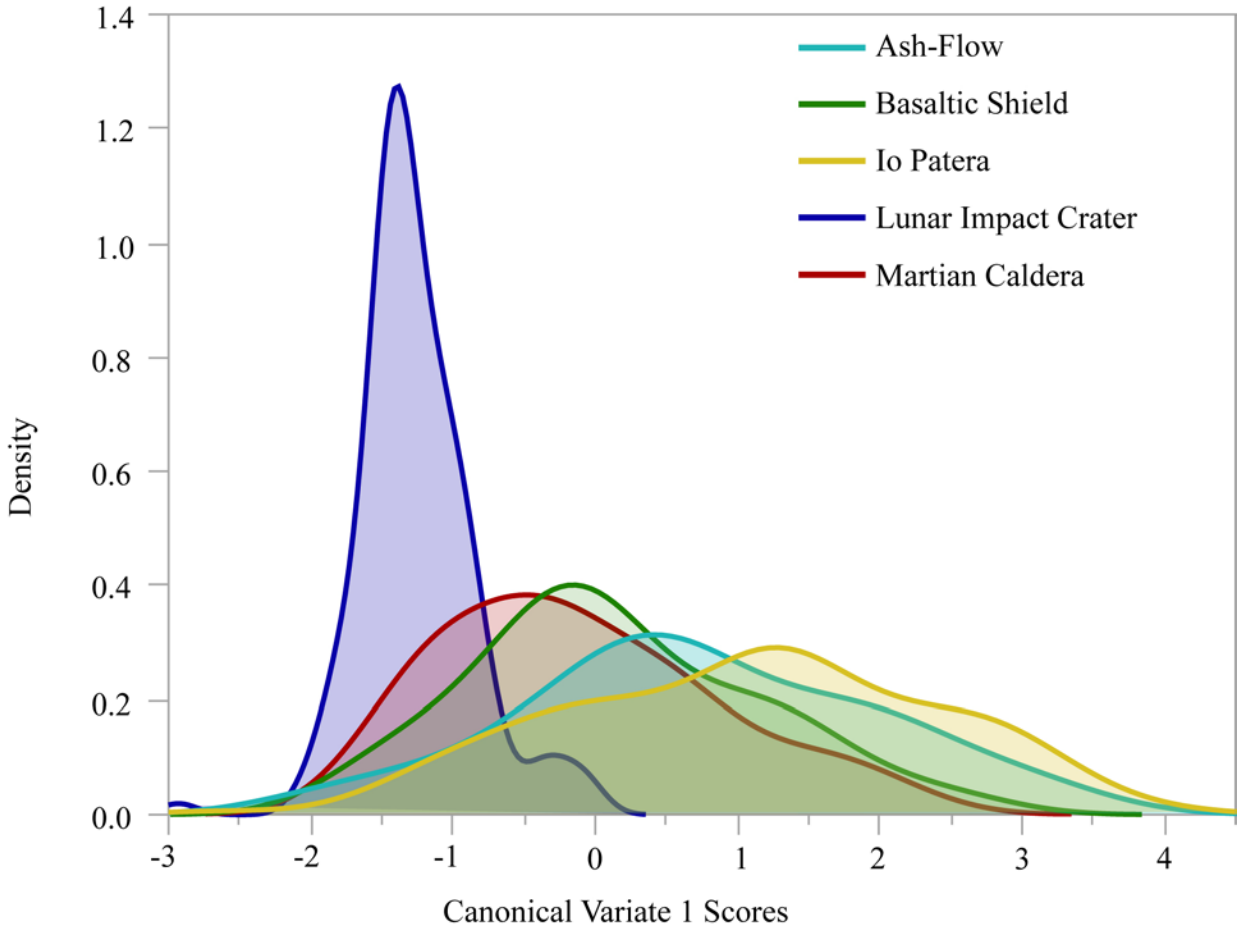

Figure 15 This plot shows a density curve distribution of the statistically significant canonical variate 1 scores from discriminant analysis of the 2nd to 5th harmonic of elliptic Fourier coefficients and the differences in these scores among craterform groups.

shield calderas are correctly assigned group membership for 26 of 35 total (74%), with 4 (11%) assigned to both the lunar impact crater group and mars caldera group, and 1 (3%) assigned membership to ionian paterae. Martian calderas are classified successfully for 19 of 24 total (79%); the remaining 5 (21%) were assigned membership to the impact crater group. Lunar impact craters have the most successful predicted classification of all the craterform groups, with 145 of 155 (94%) assigned correct membership. Of the remaining 10 impact craters, 6 (4%) are assigned to the basaltic shield group, 3 (2%) are assigned to the ash-flow caldera group, and 1 (~1%) is classified as an ionian patera.

4.5 Discriminant analysis of EFA Coefficients from the 2nd to 10th Harmonics

As shown earlier (Fig. 14), using the 2nd the 10th harmonics from analysis of the elliptic Fourier coefficients provide an effective visual representation for the complexity of shapes included in this study. The 36 elliptic Fourier coefficients representative of the 9 total harmonics, selected from *a posteriori* information, are subjected to discriminant analysis. Results from discriminant analysis are shown by Fig. 16 and Table 11 lists the *p-values* from multiple computed statistical

Table 11 Statistical significance test for the canonical variate analysis of the first 36 elliptic Fourier coefficients (10 harmonics). . The first canonical axis is shown in the first row and the additional axes follow sequentially.

Test	Value	NumDF	Prob>F
Wilks' Lambda	0.310	144	<.0001*
Pillai's Trace	0.891	144	<.0001*
Hotelling-Lawley	1.640	144	<.0001*
Roy's Max Root	1.262	36	<.0001*

tests and shows the analysis was statistically significant. Similar to the prior analysis, the ellipses shown in the plot represent 95% intervals of confidence that the group mean lies within the ellipse. These results allow the differences in classification that result when additional harmonic values are included in the analysis to be examined. All *p-values* included in Table 11 are < 0.05 and thus allow the null hypothesis, that the means of the covariates for the canonical variables are equal across all groups, to be rejected. Table 12 reveals that the first and second canonical variate axis are statistically significant and together represent 88% of the total differences in

Table 12 Statistical significance of canonical variates from analysis of 36 coefficients (2nd to 10th harmonics) from elliptic Fourier analysis.

Eigenvalue	Percent	Cum Percent	Canonical Corr	Likelihood Ratio	Prob>F
1.262	76.95	76.95	0.747	0.310	<.0001*
0.177	10.77	87.72	0.387	0.702	0.0221*
0.115	7.01	94.73	0.321	0.826	0.2981
0.086	5.27	100	0.282	0.920	0.5231

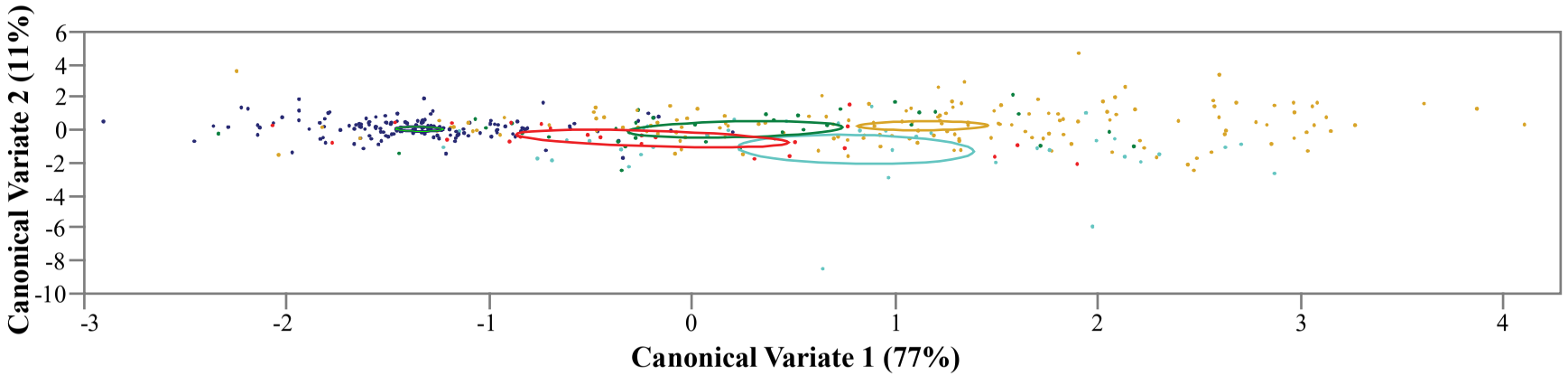

Figure 16 Discriminant analysis results for the 2nd to 10th harmonics are shown in the plot for the first 36 elliptic Fourier coefficients. Canonical variate 1 describes ~77% of the maximum difference between the craterform shape descriptors for in each group. Canonical 2 represents 10.8% of the maximal difference in shape correspondence. The ellipse for lunar impact craters is highlighted in bright green.

shape. The other canonical values have *p-values* much greater than 0.05 and thus only the *x* axis (canonical variate 1) should be considered in visual analysis of Fig. 16. In contrast to the discriminant analysis performed on coefficients of the 2nd to 5th harmonics, the shape differences represented by the first canonical variable here is lower by ~12%. Considering only statistically significant canonical variates, the cumulative percent of shape differences able to be described from discriminant analysis of the 2nd to 10th harmonics is 1.3% less than that provided by the 2nd to 5th harmonics, despite the fact that only its first canonical variate is statistically significant.

As shown by the results provided in Table 13, the discriminant model successfully classifies 90.4%, or 367 of 406 total craterforms, using the elliptic Fourier coefficients of the 10th harmonic. The predicted classifications from the canonical variate analysis of craterform shapes using the 10th harmonic, or 36 elliptic Fourier coefficients resulting from discriminant (classification) analysis are shown in Table 12 and are provided in as percentages. The predicted group membership assignments are provided in Table 14 and rates of success in the model's classification of the craterforms are provided in Table 15 The model produced from canonical variate analysis successfully classifies >99%, or 154 of the 155 total lunar impact craters included in the study, 1 (<1%) is assigned membership to the ionian patera group. Ash-flow calderas have an overall successful group classification of 84% with 32 of 38 successfully classified. Of the remaining 6 ash-flow calderas, 5 (13%) are assigned to the ionian patera group, and one (3%) ash-flow caldera is assigned to the impact crater group. Basaltic shield calderas are

Table 13 Misclassification rate of predicted group assignments from the canonical variate analysis for the 2nd to 10th EFA harmonics.

Source	Count	Number Misclassified	Percent Misclassified
Training	406	39	9.61

Table 14 Predicted group membership assignments from shape by canonical variate analysis from the EFA coefficients of the 2nd to 10th harmonics.

EFA *n*=10	Predicted Count					
Group	**Ash-Flow**	**Basaltic Shield**	**Io Patera**	**Lunar Impact**	**Mars Caldera**	**Count**
Ash-Flow	32	0	5	1	0	38
Basaltic Shield	0	31	0	4	0	35
Io Patera	1	2	138	13	0	154
Lunar Impact	0	0	1	154	0	155
Mars Caldera	0	0	6	6	12	24

Table 15 Success rates for predicted group classifications from shape by canonical variate analysis from the EFA coefficients of the 2nd to 10th harmonics.

EFA *n*=10	Predicted Count					
Group	**Ash-Flow**	**Basaltic Shield**	**Io Patera**	**Lunar Impact**	**Mars Caldera**	**Count**
Ash-Flow	**84%**	0%	13%	3%	0%	100%
Basaltic Shield	0%	**89%**	0%	11%	0%	100%
Io Patera	1%	1%	**90%**	8%	0%	100%
Lunar Impact	0%	0%	1%	**99%**	0%	100%
Mars Caldera	0%	0%	25%	25%	**50%**	100%

classified correctly for 31 of 35 total, yielding an 89% successful classification rate. The 4 remaining basaltic shield calderas (11%) are assigned to the lunar impact crater group. Of 154 total paterae, 138 (90%) are successfully classified. Of the 16 misclassified paterae, 13 (8%) are assigned to the lunar impact crater group, 2 (~1%) are assigned to the basaltic shield caldera group, and 1 (<1%) is assigned membership to the ash-flow caldera group. For the 24 martian caldera shapes examined in the study, 12 (50%) are correctly assigned group membership. Of the remaining 12 misclassified martian calderas, 6 (25%) are assigned membership to the ionian patera group, and 6 (25%) are classified as lunar impact craters.

4.6 **Multivariate analysis of Zahn and Roskies Shape Function Results**

Discriminant analysis of the Z-R shape function values is shown in Fig. 17. The points on the canonical variate plot are more widely dispersed than on the elliptic Fourier analysis plots presumably because of the greater number of variables produced by the Z-R shape function as

angles between 99 interpolated points. Table 16 shows that the results of the canonical variate analysis are statistically significant, and the null hypothesis that there is no statistical difference between the groups of craterform shapes, can be rejected. As shown in Table 17, the first two canonical variables are statistically significant at the 95% confidence level and together describe ~80% of the shape differences.

Table 17 Statistical significance test for the discriminant analysis of Z-R shape function values.

Test	Value	Prob>F
Wilks' Lambda	0.105	<.0001*
Pillai's Trace	1.608	<.0001*
Hotelling-Lawley	3.467	<.0001*
Roy's Max Root	2.047	<.0001*

Table 16 Statistical test for the canonicals resulting from discriminant analysis of Z-R shape function values.

Eigenvalue	Percent	Cum Percent	Canonical Corr	Likelihood Ratio	Prob>F
2.047	59.03	59.03	0.820	0.105	<.0001*
0.719	20.73	79.76	0.647	0.319	<.0001*
0.400	11.54	91.31	0.535	0.549	0.1679
0.301	8.69	100.00	0.481	0.768	0.5508

Canonical variate analysis results in Table 18 successfully predict group membership for ~84% of the total craterforms, misclassifying 64 out of 406 total craterform shapes. The overall misclassification rate resulting from discriminant analysis of the Z-R shape function results falls between the misclassification rates of analyses of the 2^{nd} to 5^{th} and 2^{nd} to 10^{th} harmonic orders of elliptic Fourier coefficients. While the discriminant analysis of the Z-R shape function quantities

Table 18 Overall misclassification rate from discriminant analysis of Z-R shape function.

Source	Count	Number Misclassified	Percent Misclassified
Training	406	64	15.76

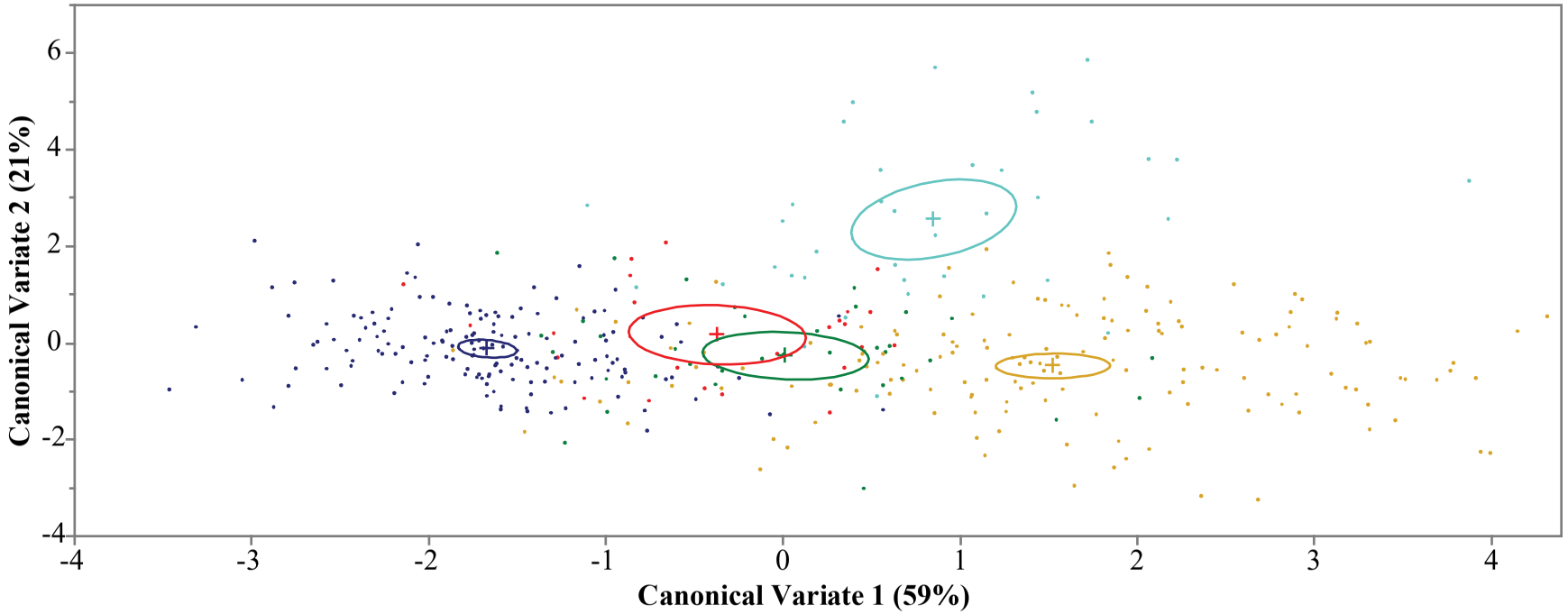

Figure 17 Canonical variate analysis of Z-R shape function multivariate radial values for the examined planetary craterforms.

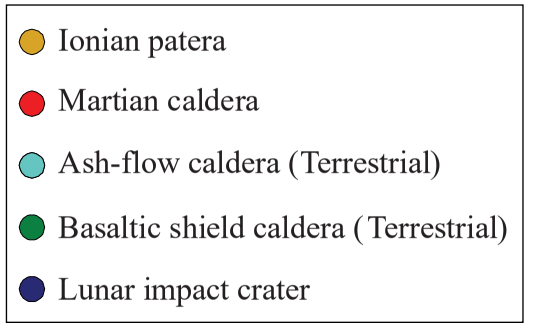

correctly classifies craterforms at an overall rate between those of the elliptic Fourier results, as shown by Table 6 and Table 12, and Z-R group membership, the most successful predicted classification rate for lunar impact craters (100%) and ionian paterae (96%), however it fails to adequately classify the remaining groups including ash-flow calderas (16%), basaltic shield calderas (51%), and martian calderas (63%) as shown by Table 19 and Table 20.

Table 19 Predicted classifications from canonical variate analysis of Z-R shape function values.

Z-R Results	Predicted Count					
Group	Ash-Flow	Basaltic Shield	Io Patera	Lunar Impact	Mars Caldera	Count
Ash-Flow	6	4	5	0	23	38
Basaltic Shield	0	18	5	0	12	35
Io Patera	0	0	148	6	0	154
Lunar Impact	0	0	0	155	0	155
Mars Caldera	0	4	3	2	15	24

Table 20 Success rate for correct group membership assignment from canonical variate analysis of Z-R shape function results.

Z-R Results	Predicted Count					
Group	Ash-Flow	Basaltic Shield	Io Patera	Lunar Impact	Mars Caldera	Count
Ash-Flow	**16%**	11%	13%	0%	61%	100%
Basaltic Shield	0%	**51%**	14%	0%	34%	100%
Io Patera	0%	0%	**96%**	4%	0%	100%
Lunar Impact	0%	0%	0%	**100%**	0%	100%
Mars Caldera	0%	17%	13%	8%	**63%**	100%

For paterae, 148 of 154 (96%) are assigned correct group membership, while the remaining 6 (4%) are assigned group membership prediction to the lunar impact crater population. For 38 ash-flow calderas, only 6 (16%) are assigned correct group membership while the majority, 23 (61%) are assigned membership to the martian caldera group. Additionally, 5 (13%) are assigned predicted membership to ionian paterae and 4 (11%) are assigned membership to the basaltic shield caldera group. Basaltic shields are classified successfully from 18 of the 35 total (51%) in this study. For the other basaltic shield calderas, 12 (34%) are assigned membership to the

martian caldera group and 5 (14%) are assigned to paterae on Io. Concerning martian calderas, the model successfully classifies 15 out of 24 (63%). Of the residual 9 martian calderas, 4 (17%) are assigned membership to the basaltic shield group, 3 (13%) are assigned to the ionian patera group, and 2 (8%) are assigned to the lunar impact crater group.

Principal component analysis was performed on the Z-R tangent angle dataset as shown in Fig. 18. The first principal axis (PC-1), or first eigenshape, represents 79.9% of shape variance among the groups of craterforms and the second principal axis (PC-2) is the second dimension of greatest variation representing 10.5% of shape variance. Thus, ~90% of shape differences and variability among the craters in the study can be represented in two-dimensions. This procedure, known as “eigenshape analysis”, shows that PCA can provide a valuable visualization tool to examine the principal variability among the craterform shapes and their respective groups.

Fig 18. shows that ionian paterae have the greatest variability among all groups and lunar impact craters have the least variability. Similar, large ellipses for ash-flow calderas and ionian paterae suggests these groups have the greatest diversity in shapes. The ellipses of basaltic shield calderas and martian calderas have similar placement in the plot, suggesting these forms vary similarly in shape.

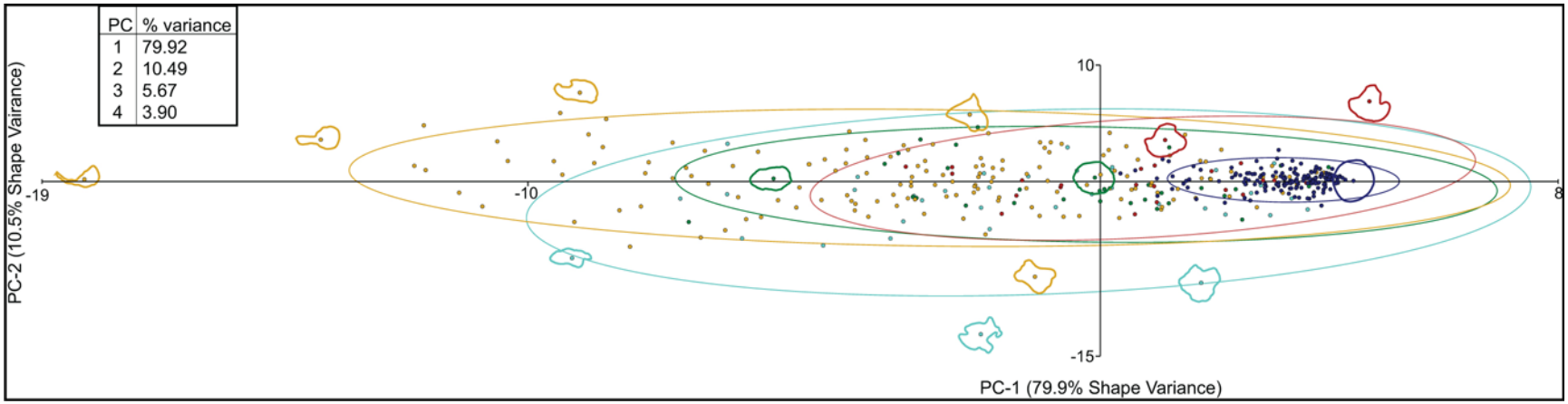

Figure 18 "Eigenshape" (principal component analysis) plot of Z-R shape function results. Goldenrod represents paterae on Io, turquoise shows ash-flow calderas, green shows basaltic shield calderas, red shows martian calderas, and navy shows lunar impact craters.

5 DISCUSSION

5.1 Craterform Shape Relationships

The findings of this study allow the null hypothesis – that groups of craterforms are unable to be differentiated from other craterforms – to be rejected with α=0.05 confidence. Shape analysis of the groups of craterforms from univariate statistical examinations of diameter (Section 4.1), circularity (Section 4.2), ellipticity (Section 4.3), as well as multivariate discriminant analysis of elliptic Fourier coefficients (Sections 4.4 and 4.5) and Z-R shape function tangent values (Section 4.6) provide consistent results to compare morphologic differences in each craterform group. As discussed below, we find that the morphology of paterae is least different to terrestrial ash-flow calderas, the morphology of basaltic shield calderas is least different to martian calderas, and the morphology of lunar impact craters are considerably different from all other compared groups.

Table 2 shows that the mean circularity and standard deviation of paterae on Io (0.81 +/- 0.12) and ash-flow calderas (0.82 +/- 0.10) are similar. Table 4 further shows that the mean ellipticity of paterae on Io (0.73 +/- 0.14) and ash-flow calderas (0.79 +/- 0.12) lie within one standard deviation, and have the lowest values (least circular) of all the craterforms studied. Martian calderas and terrestrial basaltic shield calderas are more circular and have less variability in their shapes than Ionian paterae and ash-flow calderas. Martian calderas and terrestrial basaltic shield calderas have mean circularities and standard deviations of 0.90 +/- 0.06 and 0.88 +/- 0.06

respectively. Mean ellipticities of martian calderas (0.87+/-0.07) and terrestrial basaltic shield calderas (0.83+/-0.10) are also similar. The variability indicated by standard deviation of both shape values are half that of ash-flow calderas and paterae on Io. The shapes of impact crater have a much larger mean circularity and much smaller standard deviation (0.96 +/- 0.03) as well as high ellipticity indices (also 0.96+/-0.03) despite the fact that the group includes simple, transitional, and complex crater sub-types. Furthermore, the variability in the population is half that of basaltic shield calderas and martian calderas, and a quarter of that of ash-flow calderas and Ionian paterae.

Results from univariate analysis of circularity and ellipticity using a Tukey-Kramer test show that there are statistically significant differences between the mean values for all pairwise comparisons of the craterform groups with the exception of ash-flow calderas and Ionian paterae, and basaltic shield calderas and martian calderas. Results from this test using values of ellipticity also show that there is no statistical difference between ash-flow calderas and martian calderas, and ash-flow calderas and basaltic shield calderas. While circularity and ellipticity describe similar visual properties of shape, they employ different shape information and thus provide somewhat different results when subjected to statistical testing.

Results from discriminant analysis of elliptic Fourier analysis coefficients of the 2^{nd} to 5^{th} harmonics, displayed in Table 9 and Table 10 show that lower harmonic orders describe more general information concerning the differences in shape, and that this information vary significantly between the groups. Discriminant analysis of the 2^{nd} to 10^{th} harmonic deconvolution of the elliptic Fourier coefficients produces the "best" overall classification rate (90.4%) and provides a robust model able to differentiate simple forms. Impact craters have the highest circularity and ellipticity, and paterae on Io have the lowest circularity and ellipticity.

Discriminant analysis of EFA is most powerful in its ability to achieve high classification rates among intermediate forms such as ash-flow calderas and basaltic shields (Table 14 and Table 15). Thus, discriminant analysis of EFA results, when applied at harmonic values containing a satisfactory amount of shape information, provides the strongest ability to measure complexity in shapes.

Discriminant analysis of Z-R shape function quantities was most successful in correctly classifying and assigning predicted group membership to the complex shapes of paterae on Io and the simple shapes of lunar impact craters. However, the ability of discriminant analysis using Z-R shape descriptors is substantially degraded in its ability to account for the differences that exist among the other intermediate craterforms. This method's inability to differentiate some landforms thus reveals commonalities among them. Principal component analysis of the parameters produced by Z-R shape function analysis (Fig. 18), however, does provide shape information that, while not statistically testable, reveals the major morphologic variability in the sample. PC analysis provides a visually intuitive representation of the correlation in shape among the craterform groups (Fig. 18). The plot shows 95% confidence intervals for the groups of craterforms. Lunar impact craters are highly clustered towards the center (or mean) of the plot and are easily differentiated from other forms. Basaltic shields and martian calderas plot similarly, but have different variability in shape as illustrated by the axial orientation of each ellipse. Ionian paterae and ash-flow calderas have the largest variability among the craterform groups and plot in similar orientations. These visual similarities are supportive of interpretations derived from canonical variate analysis and statistical analysis of circularity.

Classification results from canonical variate analysis of Zahn and Roskies (1972) shape function output, is shown in Table 13 and Table 14. While the analysis provides an improved

classification for paterae on Io with an overall 97% rate of success for the group and maintains a rate of 100% for successful classification of lunar impact craters, this model does not have a high success rate in distinguishing other craterforms from each other. Ash-flow caldera shapes have a 16% overall rate of successful group classification, basaltic shield calderas have a 51% successful classification rate, and martian calderas have a 63% success rate for successful group assignment. This method thus provides the strongest means of separating ionian paterae from all other craterforms, which reveals that by at least this measure, these are unique craterforms. The larger number of variables (98 angular quantities) produced by the Z-R function for each craterform may highlight that significant change in shape occurs around ionian paterae to a stronger degree than for any other craterform.

5.2 **Implications of Shape Findings for Properties of Craterforms**

Two primary relationships appear strongest among the various analyses. Only minor differences in shape exist between terrestrial ash-flow calderas and ionian paterae, and between basaltic shield calderas and martian calderas. These correlations may reveal commonalities in formation processes of craterforms. For one thing, the comparatively larger sizes of paterae on Io and terrestrial calderas might be a contributor to the minor differences in their shape.

Terrestrial ash-flow calderas are most similar to paterae on Io in shape and, possibly of greater geomorphological importance, the variability of shape (Evans, 1972). They are also comparable in size; some of the largest terrestrial calderas have diameters (or areas or perimeters) similar to Ionian paterae (Radebaugh, 1999; Davies, 2007). While the silica content of paterae on Io has been found by Keszthelyi et al. (2007) to be basaltic in composition, whereas the composition of magmas that form ash-flow calderas are much higher in silica

(rhyolitic), the mobilization of the magma by a high content of volatiles in Io's crust (Dundas, 2017) may produce similar, explosive eruption styles. It is possible that they form by similar geologic processes, or are modified over time by processes that make their shapes similar. Perhaps similar shapes result from explosive eruptive styles, crustal properties, or magmatic compositions, to name a few. Explosive eruptive styles are more likely to produce a wide range of morphologies in craterforms as they provide little time for simple geologic processes to yield a characteristic form, such as the more uniform formation processes of pit craters observed throughout the solar system (Okubo and Martel, 1998).

However, there are similarities between basalt shield calderas and paterae on Io. Both have steep walls and flat floors. Both can sustain lava lakes (Lopes et al., 2004) as indicated by dark floor materials inferred by Geissler et al. (1999) and others to be mafic silicate lavas, and are most likely basaltic in composition (Keszthelyi et al., 2007).

Minor differences in shape from analysis of basaltic shield calderas and martian calderas were revealed by this study. While it is common for the bounding morphology of these craters to be influenced by volcanic nesting, or post-formation inter-caldera collapse events, these events are also notable in ionian paterae. However, results show that paterae on Io lack shape similarities with either basaltic shield calderas or martian calderas in all examinations. Martian calderas are widely considered to be analogous to calderas on terrestrial basaltic shield volcanoes; both result from basaltic magmas and share qualitative morphologic similarities resulting from collapse style and post-formation processes (Mouginis-Mark and Robinson, 1992; Crumpler et al., 1996; Mouginis-Mark et al., 2007; Howard, 2010) as well as basic morphometric similarities (Plescia, 2004) considering rim height and crater width.

5.3 **Methodological Considerations**

A significant consideration that deserves continued question is the effect of data dimensionality reduction techniques on the results of the multivariate analysis. Data dimensionality reduction techniques have been shown to be a primary influence on differences in results from PCA in comparison to discriminant analysis (CVA) of outline analysis of bird feathers (Sheets et al., 2006) while others find little difference in results produced from CVA and PCA analysis for large multivariate datasets (Peltier et al., 2015). These types of considerations lead back to the fundamental question involved in the selection of a particular method of multivariate data analysis: What methods best describe the differences important to the geologic processes or variables investigated? While these questions vary by study, I present an overview of the methods and their effectiveness in craterform classification.

The Z-R classification model clearly portrays much different properties of shape in comparison to the elliptic Fourier derived models. While these differences in shape vary significantly from results of the EFA models, they could convey other information pertinent to currently unidentified similarities in geomorphology.

It is necessary to address the disparity among modern morphometric studies of craterforms. Some studies exclusively study craterform features on planetary bodies using metrics of ellipticity (e.g., Holohan et al., 2005) or "circularity" (e.g., Luo and Howard, 2005) as defined by Equation 3-1, and as this study shows, these two metrics can yield different conclusions as they are based on different shape properties. It may be confusing because, some studies define "circularity" using different formulas, that communicate other geomorphological information (e.g., Pike, 1976; Zuber and Parmentier, 1984). Furthermore, some studies confuse even basic geomorphological metrics such as ellipticity (axial ratio) to be the definition of "circularity"

(e.g., Schultz and Singer, 1980), which is well-founded in morphometric literature. It is helpful that the geomorphological community is able to communicate using a standard language of mathematical terminology.

5.4 **Other Implications**

Three paterae shapes: Atar, Bochica, and Unnamed patera at 11.23N, 84.74W (shown in 19) are consistent from both elliptic Fourier analysis and Z-R analysis with lunar impact craters. The shapes of these highly circular paterae on Io are sometimes indistinguishable from those of lunar impact craters. These patera could be the result of entirely different processes (e.g., impact cratering) or of a variation in the normative mechanism of patera formation. It is also possible that the near circular shapes are not "real" and the low-resolution of the images leads to a shape with less subtle deviations than in reality. These impact crater-like shapes suggest that the

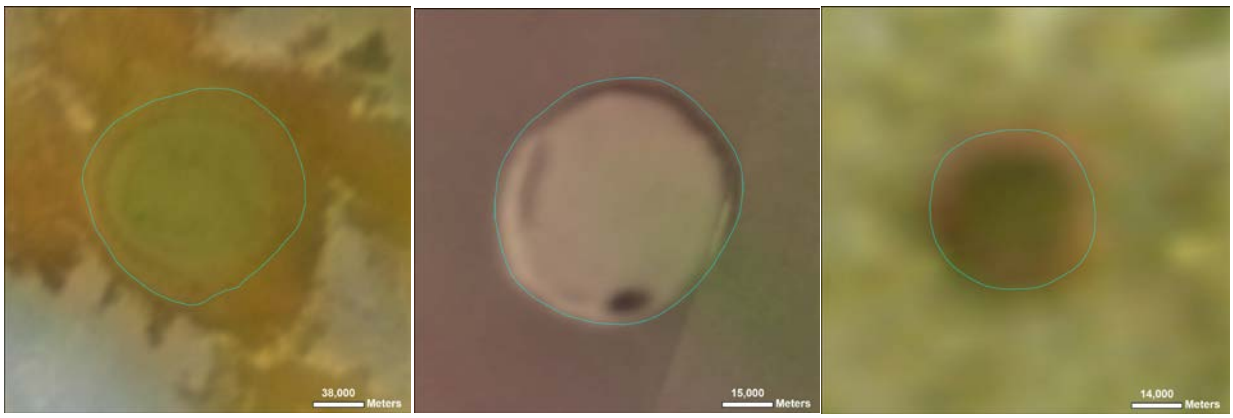

Figure 19 Highly circular paterae: Atar (left), Bochica (middle), and Unnamed patera at 11.23N, 84.74W (right) on Io classified as impact craters by statistical analysis. Dark material (~fresh lava) in B might argue against a simple crater impact origin, although without constraints on the thickness of Io's crust, impact craters could penetrate the upper lithosphere.

conclusion of Williams et al. (2011a), that no impact craters have been detected on Io's surface, is inconclusive. While the shapes of highly circular paterae are well-correlated with impact-produced craters, other mechanism common in volcanic settings, such as pit craters, could explain these features. The interpretation of the origin of these circular paterae requires a larger

craterform dataset to make supportable inferences or additional data such as higher-resolution imagery or *in-situ* observations. A mission to Io able to collect topographic data and higher resolution imagery is requisite to further our understanding of how and why patera shapes are most similar with terrestrial forms, and what implications that might have for existing models of terrestrial volcanism.

6 CONCLUSION

This study introduces a multidisciplinary approach to the quantification of planetary landforms that combines methods from systematic biology and geomorphology, two fields of the physical natural sciences that rely substantially on shape to interpret processes of origin and evolution. Outline-based approaches to geomorphologic analysis are supported by similar findings from both discriminant analysis of multivariate quantities produced from elliptic Fourier analysis and Z-R analysis. Discriminant analysis of these shape quantities shows that lunar impact craters are easily distinguished from all other craterforms, ash-flow calderas and paterae on Io are most different from all other groups in similar ways, and that basaltic shield calderas and martian calderas are the least different of all craterforms examined in the study.

The study successfully demonstrates the application of outline-based shape analysis to the study of planetary surfaces and landform morphology. The ability to quantify and examine shape information using multivariate analyses of shape enables the scientific community to investigate empirical relationships that exist between morphology and landform origin and evolution.

This study establishes the introduction of multivariate analysis to the quantification of geomorphological features in a way that allows predictive modeling and machine learning to contribute to our understanding of the role shape plays in geology. With techniques such as "eigenimage" analysis and machine learning (MacLeod, 2015; MacLeod, 2017b), computer vision, and derivative crater detection algorithms (CDA) (e.g., Stepinski et al., 2012; Emami et

al., 2015), this study displays how multivariate shape information from geomorphologic features can be used and applied to different studies.

As additional shape data is collected and the methods of this study are applied to other craterforms that have been produced by a diversity of geologic processes on planetary surfaces observed throughout the solar system, the methodology will provide clues that will enhance our understanding of the many planetary surfaces and landforms that have yet to be seen.

7 REFERENCES

Adams, D. C., Rohlf, F. J., Slice, D. E., 2013. A field comes of age: geometric morphometrics in the 21st century. Hystrix. 24**,** 7.

Andrews-Hanna, J. C., Zuber, M. T., Banerdt, W. B., 2008. The Borealis basin and the origin of the martian crustal dichotomy. Nature. 453**,** 1212-5.

Baldwin, R. B., 1963. The Measure of the Moon. University of Chicago Press.

Barker, M., Mazarico, E., Neumann, G., Zuber, M., Haruyama, J., Smith, D., 2016. A new lunar digital elevation model from the Lunar Orbiter Laser Altimeter and SELENE Terrain Camera. Icarus. 273**,** 346-355.

Barth, B., Radebaugh, J., Christiansen, E., 2009. Classification of Io's Paterae: Active vs Inactive. Lunar and Planetary Science Conference, Vol. 40.

Becker, T., Geissler, P., 2005. Galileo global color mosaics of Io. 36th Annual Lunar and Planetary Science Conference, Vol. 36.

Belton, M. J., et al., 1992. The Galileo solid-state imaging experiment. Space Science Reviews. 60**,** 413-455.

Bookstein, F. L., 1998. Morphometric Tools for Landmark Data. Biometrics. 54**,** 398.

Bookstein, F. L., 2014. Measuring and reasoning: Numerical inference in the sciences. Cambridge University Press.

Bookstein, F. L., Strauss, R. E., Humphries, J. M., Chernoff, B., Elder, R. L., Smith, G. R., 1982. A comment upon the uses of Fourier methods in systematics. Systematic Zoology. 31**,** 85-92.

Christensen, P., et al., 2009. JMARS-A Planetary GIS. AGU Fall Meeting Abstracts.

Cintala, M., Wood, C., Head, J., 1977. The effects of target characteristics on fresh crater morphology-Preliminary results for the moon and Mercury. Lunar and Planetary Science Conference Proceedings, Vol. 8, pp. 3409-3425.

Craddock, R. A., Howard, A. D., 2000. Simulated degradation of lunar impact craters and a new method for age dating farside mare deposits. Journal of Geophysical Research: Planets. 105**,** 20387-20401.

Crampton, J. S., 1995. Elliptic Fourier Shape-Analysis of Fossil Bivalves - Some Practical Considerations. Lethaia. 28**,** 179–186.

Crumpler, L. S., Head, J. W., Aubele, J. C., 1996. Calderas on Mars: characteristics, structure, and associated flank deformation. Geological Society. 110**,** 307–348.

Davies, A. G., 2007. Volcanism on Io. Cambridge University Press.

Dundas, C. M., 2017. Effects of lava heating on volatile-rich slopes on Io. Journal of Geophysical Research: Planets. 122**,** 546-559.

Edwards, C., Nowicki, K., Christensen, P., Hill, J., Gorelick, N., Murray, K., 2011. Mosaicking of global planetary image datasets: 1. Techniques and data processing for Thermal Emission Imaging System (THEMIS) multi‐spectral data. Journal of Geophysical Research: Planets. 116.

Ehrlich, R., Pharr, R. B., Healy-Williams, N., 1983. Comments on the Validity of Fourier Descriptors in Systematics: A Reply to Bookstein et al. Systematic Biology. 32**,** 202-206.

Ehrlich, R., Weinberg, B., 1970. An Exact Method for Characterization of Grain Shape. SEPM Journal of Sedimentary Research. Vol. 40**,** 1–8.

Emami, E., Bebis, G., Nefian, A., Fong, T., 2015. Automatic Crater Detection Using Convex Grouping and Convolutional Neural Networks. International Symposium on Visual Computing. Springer, pp. 213-224.

Eppler, D. T., Ehrlich, R., Nummedal, D., Schultz, P. H., 1983. Sources of Shape Variation in Lunar Impact Craters: Fourier Shape Analysis. Geological Society of America Bulletin. 94**,** 274–291.

Eppler, D. T., Nummedal, D., Ehrlich, R., 1977a. Fourier analysis of planimetric lunar crater shape-Possible guide to impact history and lunar geology. Impact and Explosion Cratering: Planetary and Terrestrial Implications, pp. 511-526.

Eppler, D. T., Nummedal, D., Ehrlich, R., 1977b. Large Scale Geologic Trends in Lunar Bedrock--Fourier Analysis of Planimetric Crater Shape. Lunar and Planetary Science Conference, Vol. 8.

Eppler, D. T., Nummedal, D., Ehrlich, R., 1978. Structural Implications of Lunar Crater Elongation. Lunar and Planetary Science Conference, Vol. 9, pp. 294-296.

Evans, I. S., 1972. General geomorphometry, derivatives of altitude, and descriptive statistics. Spatial analysis in geomorphology. 17-90.

Evans, I. S., 1986. The morphometry of specific landforms. International Geomorphology. 2**,** 105-124.

Fassett, C. I., et al., 2009. Caloris impact basin: Exterior geomorphology, stratigraphy, morphometry, radial sculpture, and smooth plains deposits. Earth and Planetary Science Letters. 285**,** 297-308.

Ferson, S., Rohlf, F. J., Koehn, R. K., 1985. Measuring Shape Variation of Two-Dimensional Outlines. Systematic Zoology. 34**,** 59.

Fisher, R. A., 1936. The use of multiple measurements in taxonomic problems. Annals of human genetics. 7**,** 179-188.

Friedman, J. H., 1989. Regularized discriminant analysis. Journal of the American statistical association. 84**,** 165-175.

Geissler, P. E., McEwen, A. S., Keszthelyi, L., Lopes-Gautier, R., Granahan, J., Simonelli, D. P., 1999. Global color variations on Io. Icarus. 140**,** 265-282.

Goudie, A., 2003. Geomorphological Techniques. Routledge, Abingdon, UK.

Greeley, R., 2011. The "Holey Tour" planetary geology field trip, Arizona. Geological Society of America Special Papers. 377–391.

Greeley, R., 2013. Introduction to Planetary Geomorphology. Cambridge University Press.

Greene, E. L., 1896. Some fundamentals of nomenclature. Science. 13-16.

Grieve, R., Robertson, P., 1979. The terrestrial cratering record: I. Current status of observations. Icarus. 38**,** 212-229.

Hammer, Ř., Harper, D., Ryan, P., 2001. PAST: Paleontological Statistics Software Package for Education and Data Analysis–Palaeontol. Electron. 4: 9pp.

Hayek, F. A., 1979. The Counter-revolution of Science: Studies on the Abuse of Reason. Liberty Press.

Hodges, C. A., Moore, H. J., 1994. Atlas of volcanic landforms on Mars. Washington: USGPO; Denver, CO: For sale by US Geological Survey, Map Division, 1994.

Holohan, E. P., Troll, V. R., Walter, T. R., Münn, S., McDonnell, S., Shipton, Z. K., 2005. Elliptical calderas in active tectonic settings: an experimental approach. Journal of Volcanology and Geothermal Research. 144**,** 119–136.

Howard, K. A., 2010. Caldera collapse: Perspectives from comparing Galápagos volcanoes, nuclear-test sinks, sandbox models, and volcanoes on Mars. GSA Today. 20**,** 4-10.

Huggett, R. J., 2016. Fundamentals of Geomorphology. Taylor & Francis.

Hughes, G. R., Mahood, G. A., 2008. Tectonic controls on the nature of large silicic calderas in volcanic arcs. Geology. 36**,** 627-630.

Keszthelyi, L., Jaeger, W., Milazzo, M., Radebaugh, J., Davies, A. G., Mitchell, K. L., 2007. New estimates for Io eruption temperatures: Implications for the interior. Icarus. 192**,** 491-502.

Kordesh, K., 1983a. Comparative Fourier grain shape analysis of meteoritic breccias and lunar soils. Lunar and Planetary Science Conference, Vol. 14, pp. 387-388.

Kordesh, K., 1983b. Fourier Grain Shape Analysis of Clasts in Achondrites Utilizing Shape Frequency Distributions. Meteoritics. 18**,** 327.

Kordesh, K., Basu, A., 1982. Roundness and sphericity of clasts in meteorites, lunar soil breccia and lunar soils. Lunar Breccias and Soils and their Meteoritic Analogs, pp. 84.

Kordesh, K., Blakely, R., Basu, A., Pachut, J., 1982. Fourier Grain Shape Analysis of Clasts in Achondrites. Meteoritics. 17**,** 236.

Kordesh, K., Mackinnon, I. D., McKay, D. S., 1983. A new classification and database for stratospheric dust particles. Lunar and Planetary Science Conference, Vol. 14. Lunar and Planetary Institute, pp. 389-390.

Kuhl, F. P., Giardina, C. R., 1982. Elliptic Fourier Features of a Closed Contour. Computer Graphics and Image Processing. 18**,** 236-258.

Lestrel, P. E., 1997. Fourier descriptors and their applications in biology. Cambridge University Press.

Lestrel, P. E., 2000. Morphometrics for the Life Sciences. World Scientific.

Lestrel, P. E., 2015. Biological Shape Analysis: Proceedings of the 3rd International Symposium, University of Tokyo, Japan, 14-17 June 2013 World Scientific.

Lipman, P. W., 1997. Subsidence of ash-flow calderas: relation to caldera size and magma-chamber geometry. Bulletin of Volcanology. 59**,** 198–218.

Loffler, G., 2008. Perception of contours and shapes: low and intermediate stage mechanisms. Vision Res. 48**,** 2106-27.

Lohmann, G. P., 1983. Eigenshape analysis of microfossils: A general morphometric procedure for describing changes in shape. Mathematical Geology. 15**,** 659–672.

Lohmann, G. P., Schweitzer, P. N., 1990. On eigenshape analysis. Proceedings of the Michigan morphometrics workshop, Vol. 145. Ann Arbor, MI: University of Michigan Museum of Zoology, pp. 166.

Lopes, R. M., et al., 2004. Lava lakes on Io: Observations of Io's volcanic activity from Galileo NIMS during the 2001 fly-bys. Icarus. 169**,** 140-174.

Losiak, A., et al., 2015. A new lunar impact crater database (updated). Lunar and Planetary Science Conference, Vol. 40.

Luo, W., Howard, A. D., 2005. Morphometric analysis of Martian valley network basins using a circularity function. Journal of Geophysical Research-Planets. 110**,** E12S13–11.

MacLeod, N., 1999. Generalizing and extending the eigenshape method of shape space visualization and analysis. Paleobiology. 25**,** 107-138.

MacLeod, N., 2002. Geometric morphometrics and geological shape-classification systems. Earth-Science Reviews. 59**,** 27–47.

MacLeod, N., 2011a. PalaeoMath 101 Part 22: Semilandmarks & RFA. Palaeontological Association Newsletter. 1–14.

MacLeod, N., 2011b. PalaeoMath 101 Part 23: Centroids, Complex Outlines & Shape Functions. Palaeontological Association Newsletter. 1–9.

MacLeod, N., 2012. PalaeoMath 101 Part 25: The Centre Cannot Hold II: Elliptic Fourier Analysis. Palaeontological Association Newsletter.

MacLeod, N., 2015. The Direct Analysis of Digital Images (Eigenimage) with a Comment on the Use of Discriminant Analysis in Morphometrics. World Scientific, pp. 156–182.

MacLeod, N., 2017a. Morphometrics: History, development methods and prospects. Zoological Systematics. 42**,** 4-33.

MacLeod, N., 2017b. On the Use of Machine Learning in Morphometric Analysis. Biological Shape Analysis: Proceedings of the 4th International Symposium, pp. 134-171.

Mahanti, P., Robinson, M. S., Humm, D. C., Stopar, J. D., 2014. A standardized approach for quantitative characterization of impact crater topography. Icarus. 241**,** 114-129.

Malin, M. C., Dzurisin, D., 1978. Modification of fresh crater landforms: Evidence from the Moon and Mercury. Journal of Geophysical Research: Solid Earth. 83**,** 233-243.

Marcus, L. F., Corti, M., Loy, A., Naylor, G. J., Slice, D. E., 1996. Advances in morphometrics. Springer Science & Business Media.

Melosh, H. J., 1989. Impact cratering: A geologic process. Research supported by NASA. New York, Oxford University Press (Oxford Monographs on Geology and Geophysics, No. 11), 1989, 253 p. 11.

Michalski, J. R., Bleacher, J. E., 2013. Supervolcanoes within an ancient volcanic province in Arabia Terra, Mars. Nature. 502**,** 47-52.

Mouginis-Mark, P. J., Harris, A. J. L., Rowland, S. K., 2007. Terrestrial analogs to the calderas of the Tharsis volcanoes on Mars. Environments on Earth: Clues to the Geology of Mars. Cambridge University Press, New York. 71-94.

Mouginis-Mark, P. J., Robinson, M. S., 1992. Evolution of the Olympus Mons Caldera, Mars. Bulletin of Volcanology. 54**,** 347-360.

Mouginis-Mark, P. J., Rowland, S. K., 2001. The geomorphology of planetary calderas. Geomorphology. 37**,** 201-223.

Neal, F. B., Russ, J. C., 2012. Measuring shape. CRC Press.

Neukum, G., König, B., Arkani-Hamed, J., 1975. A study of lunar impact crater size-distributions. Earth, Moon, and Planets. 12**,** 201-229.

Newhall, C. G., Dzurisin, D., 1988. Historical unrest at the large calderas of the world. Department of the Interior, US Geological Survey.

Okubo, C. H., Martel, S. J., 1998. Pit crater formation on Kilauea volcano, Hawaii. Journal of Volcanology and Geothermal Research. 86**,** 1–18.

Peltier, C., Visalli, M., Schlich, P., 2015. Comparison of canonical variate analysis and principal component analysis on 422 descriptive sensory studies. Food Quality and Preference. 40**,** 326-333.

Pike, R. J., 1976. Crater Dimensions from Apollo Data and Supplemental Sources. Moon. 15**,** 463-477.

Pike, R. J., 1977. Size-dependence in the shape of fresh impact craters on the Moon. Impact and Explosion Cratering: Planetary and Terrestrial Implications, pp. 489-509.

Pike, R. J., 1980. Geometric interpretation of lunar craters. Washington : U.S. Govt. Print. Off.

Pike, R. J., 2001 Scenes into numbers—facing the subjective in landform quantification. Interpreting remote sensing imagery-human factors. Lewis Publishers (CRC) Boca Raton, FL, pp. 83-114.

Pike, R. J., Clow, G. D., 1981. Revised Classification of Terrestrial Volcanoes and Catalog of Topographic Dimensions, With New Results on Edifice Volume. United States Geological Survey.

Plescia, J. B., 2004. Morphometric Properties of Martian volcanoes. Journal of Geophysical Research: Planets. 109.

Powers, M. C., 1953. A new roundness scale for sedimentary particles. Journal of Sedimentary Research. 23.

Radebaugh, J., 1999. Terrestrial Pluton and planetary caldera sizes: implications for the origin of calderas. Brigham Young University. Department of Geology.

Radebaugh, J., 2005. A Model for the Formation of Paterae on Io. 36th Annual Lunar and Planetary Science \ldots.

Radebaugh, J., Christiansen, E. H., 1999. Terrestrial Pluton Sizes: Defining the Relationship Between Planetary Calderas and Magma Chambers. Lunar and Planetary Science \ldots.

Radebaugh, J., Keszthelyi, L. P., McEwen, A. S., Turtle, E. P., Jaeger, W., Milazzo, M., 2001. Paterae on Io: A new type of volcanic caldera? Journal of Geophysical Research: Planets. 106**,** 33005-33020.

Ravine, M., Grieve, R., 1986. An analysis of morphologic variation in simple lunar craters. Journal of Geophysical Research: Solid Earth. 91.

Read, D., 1990. From multivariate to qualitative measurement: representation of shape. Human Evolution. 5**,** 417-429.

Rencher, A. C., Christensen, W. F., 2012. Methods of Multivariate Analysis.

Richtsmeier, J. T., Burke Deleon, V., Lele, S. R., 2002. The promise of geometric morphometrics. American Journal of Physical Anthropology. 119**,** 63–91.

Robbins, S. J., Achille, G. D., Hynek, B. M., 2011. The volcanic history of Mars: High-resolution crater-based studies of the calderas of 20 volcanoes. Icarus. 211**,** 1179-1203.

Rohlf, F. J., 2015. The tps series of software. Hystrix, the Italian Journal of Mammalogy. 26**,** 9-12.

Rohlf, F. J., Archie, J. W., 1984. A Comparison of Fourier Methods for the Description of Wing Shape in Mosquitoes (Diptera: Culicidae). Systematic Zoology. 33**,** 302–317.

Rohlf, F. J., Marcus, L. F., 1993. A Revolution in Morphometrics. Trends in Ecology & Evolution. 8**,** 129-132.

Sayıncı, B., Kara, M., Ercişli, S., Duyar, Ö., Ertürk, Y., 2014. Elliptic Fourier analysis for shape distinction of Turkish hazelnut cultivars. Erwerbs-Obstbau. 57**,** 1-11.

Schultz, P. H., Singer, J., 1980. A comparison of secondary craters on the Moon, Mercury, and Mars. In: Lunar and Planetary Science Conference. 11**,** 2243–2259.

Sheets, H. D., Covino, K. M., Panasiewicz, J. M., Morris, S. R., 2006. Comparison of geometric morphometric outline methods in the discrimination of age-related differences in feather shape. Frontiers in Zoology. 3**,** 15–12.

Shoemaker, E. M., 1963. Impact Mechanics at Meteor Crater, Arizona. The Moon Meteorites and Comets. 301.

Slezak, T. J., Davies, A. G., Keszthelyi, L. P., Okubo, C., Williams, D. A., 2015. Slope Stability Analysis of Scarps on Io's Surface: Implications for Upper Lithospheric Composition. Lunar and Planetary \ldots.

Slice, D., 1996. A glossary for geometric morphometrics. Advances in morphometrics. 531-551.

Smith, B. A., et al., 1977. Voyager imaging experiment. Space Science Reviews. 21**,** 103-127.

Sneath, P. H., Sokal, R. R., 1973. Numerical taxonomy. The principles and practice of numerical classification.

Stepinski, T. F., Ding, W., Vilalta, R., 2012. Detecting impact craters in planetary images using machine learning. Intelligent Data Analysis for Real-Life Applications: Theory and Practice, IGI Global. 146-159.

Tanaka, K. L., et al., 2014. Geologic map of Mars. US Geological Survey.

Thompson, D. W., 1942. On growth and form.

Veeder, G. J., Davies, A. G., Matson, D. L., Johnson, T. V., 2009. Io: Heat flow from dark volcanic fields. Icarus. 204**,** 239-253.

Venzke, E., et al., 2002. Global volcanism, 1968 to the present. Smithsonian Institution, Global Volcanism Program Digital Information Series, GVP-4 (http://www.volcano.si.edu/reports/).

Watters, W., Geiger, L., Fendrock, M., Gibson, R., Hundal, C., 2017. The role of strength defects in shaping impact crater planforms. Icarus. 286**,** 15-34.

Whitford-Stark, J., 1982. Factors influencing the morphology of volcanic landforms: An Earth-Moon comparison. Earth-Science Reviews. 18**,** 109-168.

Wilhelms, D. E., McCauley, J. F. w. s. b., Trask, N. J., 1987. The geologic history of the Moon. Professional Paper.

Williams, D. A., et al., 2009. The circum-Hellas volcanic province, Mars: overview. Planetary and Space Science. 57**,** 895-916.

Williams, D. A., et al., 2011a. Geologic Map of Io. 1–29.

Williams, D. A., et al., 2011b. Volcanism on Io: New insights from global geologic mapping. Icarus. 214**,** 91-112.

Wood, C., Head, J., Cintala, M., 1977. Crater degradation on Mercury and the moon-Clues to surface evolution. Lunar and Planetary Science Conference Proceedings, Vol. 8, pp. 3503-3520.

Zahn, C. T., Roskies, R. Z., 1972. Fourier Descriptors for Plane Closed Curves. IEEE Transactions on Computers. C-21**,** 269-281.

Zimbelman, J. R., 2001. Image resolution and evaluation of genetic hypotheses for planetary landscapes. Geomorphology. 37**,** 179-199.

Zuber, M. T., Parmentier, E. M., 1984. A Geometric Analysis of Surface Deformation - Implications for the Tectonic Evolution of Ganymede. Icarus. 60**,** 200-210.